Single-qubit gates beyond the rotating-wave approximation for strongly anharmonic low-frequency qubits

Martijn F. S. Zwanenburg [1,*] Siddharth Singh [1] Eugene Y. Huang [1] Figen Yilmaz [1] Taryn V. Stefanski [1,2] Jinlun Hu [1] Piranavan Kumaravadivel [3] and Christian Kraglund Andersen [1,†]

[1] *QuTech and Kavli Institute of Nanoscience, Delft University of Technology, 2628 CJ Delft, The Netherlands*

[2] *Quantum Engineering Centre for Doctoral Training, H. H. Wills Physics Laboratory and Department of Electrical and Electronic Engineering, University of Bristol, Bristol BS8 1FD, United Kingdom*

[3] *QuTech and Netherlands Organization for Applied Scientific Research (TNO), 2628 CJ Delft, The Netherlands*

(Received 8 April 2025; accepted 17 November 2025; published 12 December 2025)

In many quantum platforms, single-qubit gates are applied using a linear drive resonant with the qubit transition frequency, which is often theoretically described within the rotating-wave approximation (RWA). However, for fast gates on low-frequency qubits, the RWA may not hold and we need to consider the contribution from counterrotating terms to the qubit dynamics. The inclusion of counterrotating terms into the theoretical description gives rise to two challenges. First, it becomes challenging to analytically calculate the time evolution as the Hamiltonian is no longer self-commuting. Moreover, the time evolution now depends on the carrier phase such that, in general, every operation in a sequence of gates is different. In this work, we derive and verify a correction to the drive pulses that minimizes the effect of these counterrotating terms in a two-level system. We then derive a second correction term that arises from noncomputational levels for a strongly anharmonic system. We experimentally implement these correction terms on a fluxonium superconducting qubit, which is an example of a strongly anharmonic, low-frequency qubit for which the RWA may not hold, and demonstrate how fast, high-fidelity single-qubit gates can be achieved without the need for additional hardware and calibration complexities.

DOI: 10.1103/z62h-kcnh

I. INTRODUCTION

Single-qubit operations lie at the heart of many potential applications of quantum computing [1,2]. In many quantum computing architectures, such as nitrogen-vacancy centers [3], quantum dots [4,5], trapped ions [6,7], and superconducting circuits [8,9], these operations are implemented using linearly polarized signals. This linear drive signal consists of two components: one that rotates in the same direction as the qubit on the Bloch sphere and one that rotates in the opposite direction, which are denoted as the corotating and counterrotating terms, respectively. The theoretical description of these operations often relies on making the rotating-wave approximation (RWA), in which the counterrotating terms are dropped resulting in a Hamiltonian that is exactly solvable when the drive strength is time-independent or when the drive frequency is on resonance with the qubit transition frequency [10,11]. Making the RWA is justified when the ratio between the drive strength and the drive frequency is small. There are two dominant error channels when considering the implementation of such a drive signal on a realistic system: the shift in qubit frequency known as the ac Stark shift and leakage to levels outside the computational subspace [12–14]. Common ways to suppress these error channels include the derivative removal by adiabatic gate (DRAG) technique [15,16], DRAG-inspired techniques [17–19], and numerical gradient-descent optimization techniques [20,21].

When the ratio between the drive strength and the drive frequency is increased and the RWA becomes invalid, the dynamics of the system becomes richer in nature [22–28]. For example, the time evolution now depends on the phase of the carrier signal such that it depends on the absolute time at which the drive signal is applied. Furthermore, there is no straightforward way to analytically derive the time evolution, making it challenging to compute the pulse parameters that maximize the gate fidelity.

Recently, Ref. [25] proposed and implemented two methods, using a superconducting qubit, to mitigate these challenges. The first method uses a circularly polarized drive signal, which is implemented by driving the qubit simultaneously through its charge and phase degree of freedom. The second method implements commensurate gates, in which the gate duration is fixed to half-integer multiples of the qubit's Larmor period, which regularizes the errors. A drawback of these methods is that they both require nonconventional hardware: For the circularly polarized drive, two drive lines are required per qubit, and for the commensurate gates, a signal generator with a very high sampling rate is required.

In this work, we show analytically, numerically, and experimentally that it is possible to achieve low gate errors by using

*Contact author: m.f.s.zwanenburg@tudelft.nl

†Contact author: c.k.andersen@tudelft.nl

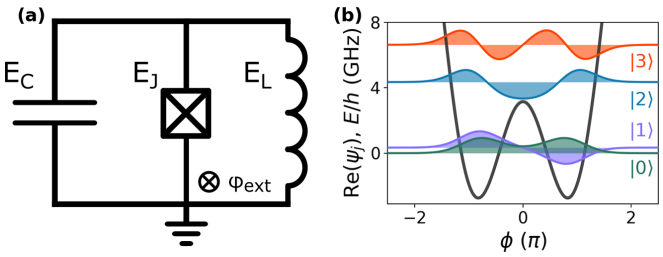

FIG. 1. (a) Circuit diagram of the fluxonium qubit. (b) Potential and the wavefunctions offset by the eigenenergies of the first four levels for $E_C/h = E_L/h = 1$ GHz and $E_J/h = 5$ GHz at the sweet spot $\varphi_{\text{ext}} = 0.5$.

conventional hardware and pulse shaping techniques. We employ the Magnus-Taylor expansion introduced in Ref. [29] to derive optimal pulse shapes for a two-level system undergoing a drive beyond the RWA. Additionally, we derive and verify a second correction term arising from noncomputational levels (NCLs) for a strongly anharmonic, low-frequency system. Finally, we use the derived pulse shapes and the understanding of non-RWA dynamics developed in this work to formulate deterministic experimental calibration protocols. Numerically, we find that, using relatively straightforward calibration procedures and for the system studied in this work, it is possible to achieve coherent error rates averaged over π and $\pi/2$ gates below 10^{-6} for gate durations as short as 2.64 Larmor periods.

While the general theory in this work is applicable to any strongly anharmonic, low-frequency system, we are specifically inspired by the fluxonium qubit as one such example [30]. A fluxonium qubit consists of a capacitor shunted by a single Josephson junction and a linear inductor characterized by the energies E_C, E_J, and E_L, respectively. The circuit diagram of a fluxonium qubit is shown in Fig. 1(a), and the Hamiltonian of such a circuit is given by

$$\hat{H} = 4E_C\hat{n}^2 + \tfrac{1}{2}E_L\hat{\phi}^2 - E_J\cos(\hat{\phi} - 2\pi\varphi_{\text{ext}}). \tag{1}$$

Here, $\hat{n}$ and $\hat{\phi}$ are the number-of-Cooper-pairs and phase operators, respectively, and $\varphi_{\text{ext}} = \Phi_{\text{ext}}/\Phi_0$ is the reduced external flux, with Φ_{ext} the external flux and Φ_0 the magnetic flux quantum. When the fluxonium is tuned to its sweet spot at $\varphi_{\text{ext}} = 0.5$, the potential mimics a double-well potential, where the wavefunctions of the $|0\rangle$ and $|1\rangle$ states are symmetric and antisymmetric superpositions of states living in the left and right wells. The potential and wavefunctions for a fluxonium with example parameters $E_C/h = E_L/h = 1$ GHz and $E_J/h = 5$ GHz are computed using `scqubits` and shown in Fig. 1(b) [31,32]. The qubit transition frequency of a typical fluxonium at its operating point is in the 100–1000 MHz range [25,33–45], but can also be in the 1–100 MHz range by designing a heavier fluxonium [46–48]. Since single-qubit gate durations on fluxonium qubits are typically in the 10–100 ns range, resulting in drive strengths in the 10–100 MHz range, they are an ideal platform to investigate non-RWA effects in single-qubit operations.

II. THEORY: SINGLE-QUBIT GATES BEYOND THE RWA

Our description of single-qubit gates starts with a general drive Hamiltonian for a two-level system [49]:

$$H/\hbar = \omega_q\,|1\rangle\langle 1| + \mathcal{D}(t)(|0\rangle\langle 1| + |1\rangle\langle 0|), \tag{2}$$

where ω_q is the qubit frequency and $\mathcal{D}(t)$ is the drive signal defined by

$$\begin{aligned}\mathcal{D}(t) &= \text{Re}\,(\mathcal{E}(t))\cos(\omega_d t + \phi) + \text{Im}(\mathcal{E}(t))\sin(\omega_d t + \phi),\\ \mathcal{E}(t) &= e^{i\theta}(\mathcal{E}_I(t) + i\mathcal{E}_Q(t)).\end{aligned} \tag{3}$$

Here, ω_d is the drive frequency, ϕ the phase of the carrier signal, θ the angle of the rotation axis with respect to the X axis of the Bloch sphere, and $\mathcal{E}_I(t)$ and $\mathcal{E}_Q(t)$ the in-phase and quadrature pulse envelopes, respectively. For now, we restrict ourselves to X rotations by setting $\theta = 0$. We proceed to transform the Hamiltonian into the rotating frame $\tilde{H}(t) = V(t)H(t)V^\dagger(t) + i\dot{V}(t)V^\dagger(t)$, with $V(t) = \exp(i(\omega_d t + \phi)|1\rangle\langle 1|)$ to obtain

$$\begin{aligned}\tilde{H}(t)/\hbar &= -\frac{\Delta}{2}\sigma_z + A_I(t)\sigma_x + A_Q(t)\sigma_y,\\ A_I(t) &= \frac{1}{2}(\mathcal{E}_I(t)(1 + \cos(2\omega_d t + 2\phi))\\ &\quad + \mathcal{E}_Q(t)\sin(2\omega_d t + 2\phi)),\\ A_Q(t) &= \frac{1}{2}(\mathcal{E}_Q(t)(1 - \cos(2\omega_d t + 2\phi))\\ &\quad + \mathcal{E}_I(t)\sin(2\omega_d t + 2\phi)),\end{aligned} \tag{4}$$

with $\Delta = \omega_q - \omega_d$ the detuning between the qubit and drive frequency. The in-phase and quadrature components of the drive signal both contribute to one stationary term and two nonstationary terms that oscillate at $2\omega_d$. If we invoke the RWA and drop the oscillating terms, we arrive at the RWA Hamiltonian:

$$\tilde{H}_{\text{RWA}}(t)/\hbar = -\frac{\Delta}{2}\sigma_z + \frac{1}{2}(\mathcal{E}_I(t)\sigma_x + \mathcal{E}_Q(t)\sigma_y). \tag{5}$$

Here, we are interested in determining the pulse parameters that implement a given operation with maximum fidelity. Specifically, we consider an operation applied from $t = 0$ to $t = t_g$, with t_g the gate duration. If the RWA holds, it is straightforward to derive the pulse parameters that implement any arbitrary rotation on the Bloch sphere. For example, for an X_π gate, we set $\Delta = \mathcal{E}_Q = 0$ and $\int_0^{t_g} dt\mathcal{E}_I(t) = \pi$. In contrast, if the RWA does not hold, there are two factors that significantly complicate the description of single-qubit gates. First, the time evolution is no longer independent of the carrier phase ϕ, such that the time evolution depends on the absolute time at which the gate is applied. Second, the non-RWA Hamiltonian $\tilde{H}$ is not self-commuting such that an analytical expression for the time evolution is challenging to obtain. Even if an (approximate) expression can be computed, it may be challenging to derive the ideal pulse parameters from that solution.

To resolve these challenges, we make use of the methods introduced in Ref. [29]. Rather than computing the time evolution over the full duration of the operation, the time interval on which the time evolution is calculated is restricted to Magnus

intervals $t_{m,n} = [t_0 + (n-m)t_c, t_0 + nt_c]$. Here, $t_c = \pi/\omega_d$ is the Magnus period, which is the period of the nonstationary terms in the Hamiltonian, and m and n are positive integers such that the time interval $t_{m,n}$ contains m Magnus periods. As will be shown, it is possible to derive corrections for the non-RWA terms in the Hamiltonian by restricting to the Magnus intervals $t_{m,n}$. To derive these corrections, the key idea is to intersect the non-RWA and RWA time evolutions on these Magnus intervals:

$$\mathcal{T}\exp\left(-\frac{i}{\hbar}\int_{t_0+(n-m)t_c}^{t_0+nt_c} d\tau \tilde{H}_{\mathrm{RWA}}(\tau, \mathcal{P}_{\mathrm{RWA}})\right) = \mathcal{T}\exp\left(-\frac{i}{\hbar}\int_{t_0+(n-m)t_c}^{t_0+nt_c} d\tau \tilde{H}(\tau, \mathcal{P})\right), \tag{6}$$

with $\mathcal{T}$ the time-ordering operator, and the dependence of both Hamiltonians on the pulse parameters is shown explicitly. $\mathcal{P}_{\mathrm{RWA}}$ are the ideal pulse parameters if the RWA holds exactly and $\mathcal{P}$ are the to-be-derived pulse parameters that intersect the non-RWA and RWA time evolutions on the specified interval. Notice that, unless the gate is commensurate (i.e., the gate duration is an exact integer multiple of the Magnus period), Eq. (6) cannot capture the full evolution from $t = 0$ to $t = t_g$. However, we can maximize the interval on which the RWA and non-RWA evolutions are equivalent by satisfying Eq. (6) from t_0 to $t = t_0 + N_c t_c$, with $N_c = \lfloor \frac{t_g - t_0}{t_c} \rfloor$ the number of Magnus periods during the operation, where $\lfloor\cdot\rfloor$ is the floor function. If Eq. (6) is satisfied, the non-RWA Hamiltonian implements the same time evolution $U(t_0, t_0 + N_c t_c)$ as the RWA Hamiltonian. Since the RWA Hamiltonian implements the desired operation $U(0, t_g)$ with unit fidelity, we expect the pulse parameters $\mathcal{P}$ that solve Eq. (6) to also minimize the error in the full non-RWA time evolution from $t = 0$ to $t = t_g$. This expectation is based on the assumption that the effect of the non-RWA terms is small on the uncorrected time intervals with $t \in [0, t_0] \cup [N_c t_c + t_0, t_g]$. We expect this to be the case for sufficiently long gates as the uncorrected intervals are then small compared to the total time evolution. Consequently, we expect this framework to break down as N_c approaches 1.

There are two choices for n and m for which Eq. (6) is satisfied on the interval $t \in [t_0, t_0 + N_c t_c]$. We can either satisfy Eq. (6) for all n and $m = 1$ such that it is satisfied for all Magnus intervals during the gate. The other choice is to directly integrate over N_c Magnus periods by setting $m = n = N_c$. Here, we will focus on the latter choice as we find that it allows for a more straightforward derivation of the correction terms. We note that we will keep the integration bounds in the their general form, as we will touch upon different choices for n and m in later parts of this work.

To derive the pulse parameters $\mathcal{P}$ that satisfy Eq. (6), we Magnus expand the non-RWA time evolution, of which the first two terms are given by [50,51]

$$\overline{H}^{(0)} = -\frac{i}{\hbar}\int_{b_-}^{b_+} dt_1 H(t_1),$$
$$\overline{H}^{(1)} = -\frac{1}{2\hbar^2}\int_{b_-}^{b_+} dt_1 \int_{b_-}^{t_1} dt_2 [H(t_1), H(t_2)], \tag{7}$$

such that we can approximate the time evolution over the Magnus intervals $t_{m,n}$ by

$$U(b_+, b_-) = \mathcal{T}\exp\left(-\frac{i}{\hbar}\int_{b_-}^{b_+} d\tau H(\tau)\right) = \exp(\overline{H}), \quad \overline{H} = \sum_{k=0}^{\infty} \overline{H}^{(k)}. \tag{8}$$

Here, we have defined $b_- = t_0 + (n-m)t_c$ and $b_+ = t_0 + nt_c$. The time-ordering operator for the RWA time evolution can typically be dropped as the RWA Hamiltonian $\tilde{H}_{\mathrm{RWA}}$ commutes with itself for $\Delta = \mathcal{E}_Q = 0$ (in an appropriate frame). Using Eqs. (4)–(8), it is possible to derive expressions for the ideal pulse parameters. In the following sections, we will derive and numerically verify these expressions for the zeroth-order and first-order Magnus expansion terms, which we will refer to as the zeroth/first-order Magnus approximation.

A. Zeroth-order Magnus expansion

While the formalism derived here is applicable to any smooth pulse envelope, it is convenient to explicitly define the pulse envelope $\mathcal{E}_I(t)$. In this work, we focus specifically on the cosine pulse envelope defined as

$$\mathcal{E}_I(t) = \Omega_I s_I(t) = \frac{\Omega_I}{2}\left(1 - \cos\left(\frac{2\pi}{t_g}t\right)\right). \tag{9}$$

Here, Ω_I is the drive strength and $s_I(t)$ defines the shape of the in-phase pulse envelope. Using Eqs. (4)–(8), we obtain three requirements for the pulse parameters in the zeroth-order Magnus approximation:

$$\text{(i)} \quad \int_{b_-}^{b_+} dt_1 \frac{-\Delta}{2} = 0,$$
$$\text{(ii)} \quad \int_{b_-}^{b_+} dt_1 A_Q(t_1, \mathcal{P}) = 0,$$
$$\text{(iii)} \quad \int_{b_-}^{b_+} dt_1 A_I(t_1, \mathcal{P}) = \int_{b_-}^{b_+} dt_1 \frac{\mathcal{E}_I(t_1, \mathcal{P}_{\mathrm{RWA}})}{2}. \tag{10}$$

Requirement (i) is straightforwardly satisfied by setting $\Delta = 0$. By Taylor expanding the pulse envelopes, we find that we can satisfy requirement (ii) by defining the quadrature pulse envelope as

$$\mathcal{E}_Q(t) = \lambda\frac{\partial \mathcal{E}_I(t)}{\partial t} = \lambda\Omega_I\frac{\pi}{t_g}\sin\left(\frac{2\pi}{t_g}t\right), \tag{11}$$

with λ defining the relative drive strength of the quadrature drive signal, which we will refer to as the pulse proportionality parameter (PPP). A full derivation for the quadrature pulse envelope is provided in Appendix A. We find that requirement (iii) can be satisfied independently of the shape of the quadrature pulse envelope. By computing the integrals in requirements (ii) and (iii), we obtain closed-form expressions for the PPP λ and the drive

strength Ω_I:

$$\lambda = \frac{\sum_{k=0}^{\infty}\left(\frac{1}{2\omega_d}\right)^{k+1}\gamma_2(k,\beta)\left[\frac{\partial^k s_I(t_1)}{\partial t_1^k}\right]_{t_1=b_-}^{b_+}}{s_I(b_+)-s_I(b_-)-\sum_{k=0}^{\infty}\left(\frac{1}{2\omega_d}\right)^{k+1}\gamma_1(k,\beta)\left[\frac{\partial^{k+1} s_I(t_1)}{\partial t_1^{k+1}}\right]_{t_1=b_-}^{b_+}}, \tag{12a}$$

$$\frac{\Omega_I}{\Omega_{I,\mathrm{RWA}}} = \frac{\int_{b_-}^{b_+} dt_1 s_I(t_1)}{\int_{b_-}^{b_+} dt_1 s_I(t_1)+\sum_{k=0}^{\infty}\left(\frac{1}{2\omega_d}\right)^{k+1}\left\{\gamma_1(k,\beta)\left[\frac{\partial^k s_I(t_1)}{\partial t_1^k}\right]_{t_1=b_-}^{b_+}-\lambda\gamma_2(k,\beta)\left[\frac{\partial^{k+1} s_I(t_1)}{\partial t_1^{k+1}}\right]_{t_1=b_-}^{b_+}\right\}}. \tag{12b}$$

Here, $\Omega_{I,\mathrm{RWA}}$ is the ideal drive strength for the RWA Hamiltonian and we have defined

$$\gamma_1(k,\beta) = (-1)^{\lfloor\frac{k}{2}\rfloor}(\chi_+(k)\sin(\beta)+\chi_-(k)\cos(\beta)),$$
$$\gamma_2(k,\beta) = (-1)^{\lfloor\frac{k+1}{2}\rfloor}(\chi_+(k)\cos(\beta)+\chi_-(k)\sin(\beta)), \tag{13}$$

with $\beta = 2\omega_d t_0 + 2\phi$ and $\chi_\pm(k) = \frac{1\pm(-1)^k}{2}$. As apparent from Eq. (12), the expressions for the pulse parameters are given by an infinite series. The magnitude of the terms in these sums scales with $(\pi/\omega_d t_g)^k = (t_c/t_g)^k$, since $\frac{\partial^k s_I(t)}{\partial t^k} \sim (2\pi/t_g)^k$ [as seen from Eq. (9)]. As we are specifically interested in operations for which the drive strength approaches the same order of magnitude as the drive frequency, i.e., $1 \lesssim t_g/t_c \lesssim 10$, convergence of these infinite series might be slow, so it is important to truncate these sums at sufficiently high k. For $t_g < t_c$, the ideal pulse parameters calculated in Eq. (12) are undefined since there are no Magnus intervals to integrate over in Eq. (6).

As apparent from Eqs. (12) and (13), the ideal pulse parameters depend on the carrier phase ϕ through the parameter β. This dependence is problematic, since every gate in a sequence of operations generally has a different starting carrier phase, and varying the pulse parameters for each gate is highly impractical. Therefore, the ideal pulse parameters have to be defined as an average of the expressions in Eq. (12) over the carrier phase ϕ. From this, we intuitively understand how the breakdown of the RWA causes the average gate error to increase: When the RWA becomes increasingly invalid, the dependence of the time evolution on the carrier phase increases, which increases the variance of the pulse parameters calculated in Eq. (12) such that the pulse parameters averaged over the carrier phase no longer result in low gate errors for all carrier phases. The pulse parameters also depend on the start of the integration window t_0. This parameter, unlike the carrier phase, does not represent a physical parameter from the drive pulse. Instead, we are free to choose t_0 in Eq. (12), where this choice is represented through the parameters β and $b_\pm$. This indicates that for each carrier phase ϕ there may exist a range of ideal pulse parameters corresponding to different choices of t_0 rather than one unique solution.

Two open questions remain: Can the dependence of the ideal pulse parameters on the carrier phase ϕ be eliminated, and how do we choose β and $b_\pm$ or equivalently the start of the integration window t_0? As detailed in Appendix B, we can leverage the freedom to choose these parameters to derive exact algebraic solutions for Ω_I and λ in Eq. (12). Strikingly, we find that, by simply setting $\lambda = 1/2\omega_d$ and $\Omega_I = \Omega_{I,\mathrm{RWA}}$, the non-RWA terms in the zeroth-order Magnus approximation are corrected independently of the carrier phase and over the full time evolution from $t = 0$ to $t = t_g$ rather than only over Magnus intervals. This solution corresponds to setting $\beta = 0$ or by using a symmetric integration window around $t = t_g/2$ such that $t_0 = (t_g - N_c t_c)/2$. We highlight that these solutions exist as long as the pulse envelopes are analytic on the interval $t \in [0, t_g]$ and if $s_I(0) = s_I(t_g) = 0$. For the symmetric integration windows, it is additionally required that each even (odd) kth time derivative of $s_I(t)$ is symmetric (antisymmetric) around $t = t_g/2$. We emphasize that these solutions only exist for the specified parameters, and that we have not been able to derive similar solutions in higher-order Magnus approximations. Therefore, the algebraic solution is only used in the zeroth-order Magnus approximation and for the specified parameters, and in all other situations the terms in Eq. (12) have to be computed directly, which we will refer to as the truncated series solution.

In Fig. 2, we investigate the accuracy of the correction terms for the zeroth-order Magnus expansion for $\omega_{01}/2\pi = \omega_d/2\pi = 80$ MHz. Specifically, we compute the error E between the desired RWA time evolution and zeroth-order Magnus expanded non-RWA time evolution for varying pulse parameters. The error between two time evolutions U and V is defined as $E = 1 - F$, with F the average gate fidelity, which, under the assumption that U and V are unitary, can be expressed as [52,53]

$$F(U,V) = \tfrac{1}{6}(2 + \mathrm{Tr}(UV^\dagger)\mathrm{Tr}(U^\dagger V)). \tag{14}$$

In Fig. 2(a), the error is plotted as a function of the gate duration for $\phi = t_0 = \beta = 0$. First, we naively use the RWA pulse parameters in the zeroth-order Magnus expanded non-RWA Hamiltonian, which we refer to as the uncorrected pulse parameters, i.e., $\Omega_I = \Omega_{I,\mathrm{RWA}}$ and $\lambda = 0$. For these pulse parameters, the error increases exponentially as the gate duration shortens. Whenever the gate is commensurate, i.e., $t_g = nt_c$ for an integer n, the error for the uncorrected pulse parameters is zero since the oscillating non-RWA terms in the Hamiltonian integrate exactly to zero. For the corrected parameters, the algebraic solution to Eq. (12) (solid lines) and the truncated series solution (dashed lines) are plotted. For the truncated series solution, the pulse parameters are computed up to 15th order in t_c/t_g, i.e., $k \leqslant 14$. For the algebraic parameters, the error is negligible and independent of the gate duration. For the truncated series solution, the error increases suddenly for $t_g < 2t_c$, which is ascribed to the truncation error due to the aforementioned convergence rate of the infinite series in Eq. (12). In Fig. 2(b), we plot the error as a function of time for a 20 ns gate with the same parameters as in Fig. 2(a) for the uncorrected and corrected pulse parameters. We see that, as detailed in Appendix B, the corrected time evolution intersects

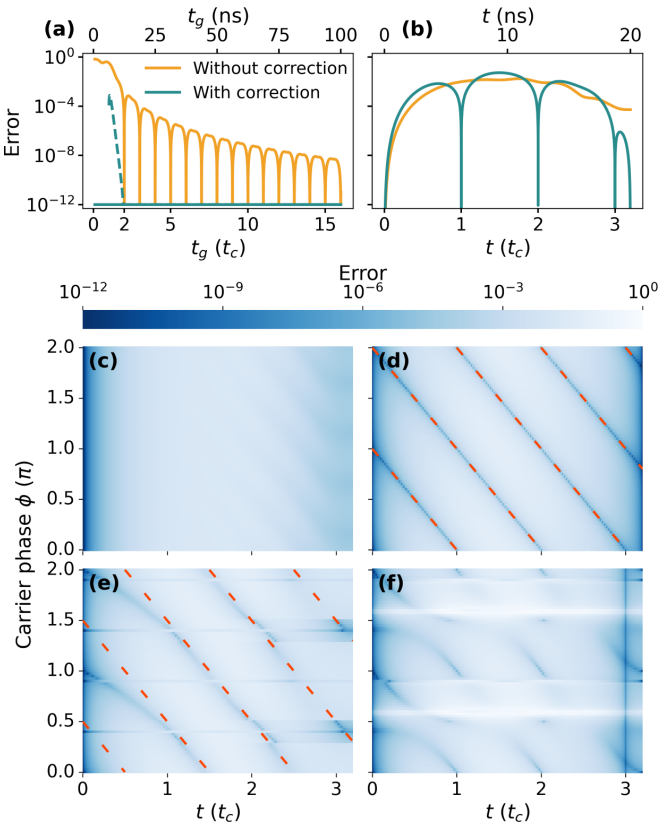

FIG. 2. Error between the zeroth-order Magnus expanded non-RWA time evolution and the desired RWA time evolution for $\omega_{01}/2\pi = \omega_d/2\pi = 80$ MHz. Errors are truncated at 10^{-12} for visibility purposes. (a) Gate error as a function of the gate duration t_g. The uncorrected pulse parameters correspond to setting $\mathcal{P} = \mathcal{P}_{\mathrm{RWA}}$. The solid corrected line corresponds to the algebraic result, i.e., $\Omega_I = \Omega_{I,\mathrm{RWA}}$ and $\lambda = 1/2\omega_d$, and the dashed line corresponds to the truncated series solution for $k \leqslant 14$. (b) Corrected and uncorrected errors as a function of instantaneous time t for a 20 ns gate. In panels (a) and (b), the carrier phase $\phi = 0$. (c)–(f) Heatmaps of the same simulation as in panel (b) as a function of the carrier phase. Panels (c) and (d) show the error for the uncorrected pulse parameters and algebraic result, respectively. Panels (e) and (f) show the results for the truncated series solution with $k \leqslant 14$ corresponding to the parameter choices $\beta = \pi$ and $t_0 = 0$, respectively. The dashed lines in panels (d) and (e) indicate the times for which $t = t_0 + nt_c$.

the RWA evolution every Magnus period as well as at the end of the gate.

In Figs. 2(c)–2(f), we perform the same simulations as in Fig. 2(b) as a function of the carrier phase ϕ. In Figs. 2(c) and 2(d), we compute the error for the uncorrected pulse parameters and the algebraic solution, respectively. As expected, for the uncorrected pulse parameters, the RWA and non-RWA evolutions do not intersect. For the algebraic pulse parameters, the evolutions intersect every Magnus period and at $t = t_g$. The absolute time at which the evolutions intersect varies, since a change in carrier phase ϕ requires a shift in the start of the integration window t_0 as we require $\beta = 2\omega_d t_0 + 2\phi = 0$ for the algebraic solution. In Fig. 2(e), we use the truncated series solution corresponding to $\beta = \pi$, where we observe that low errors are only achieved when $t_0 \approx 0$ corresponding to $\phi \approx \beta/2 = \pi/2$. For other values of the carrier phase, $t_0 \neq 0$ such that the RWA and non-RWA evolutions have already diverged before $t = t_0$ and will not intersect anymore. In Fig. 2(f), we therefore fix $t_0 = 0$ such that $\beta = 2\phi$. Notice that this implies that we re-evaluate the correction terms using Eq. (12) for each horizontal linecut in this figure. As expected, the RWA and non-RWA time evolutions intersect at $t = N_c t_c$, but diverge in the uncorrected time interval $t \in [N_c t_c, t_g]$.

Even though we have now only considered the zeroth-order Magnus expansion, the results in Fig. 2 already provide us with a clear intuition for the ideal pulse parameters beyond the RWA. For each gate, the carrier phase increments with $w_d t_g$ with respect to the previous gate, such that each gate is represented by a different horizontal linecut in Fig. 2. Therefore, we conclude that high-fidelity operations beyond the RWA are enabled through the existence of the exact algebraic solution shown in Fig. 2(d), as this is the only solution for which the pulse parameters are independent of the carrier phase and the error is low for each carrier phase.

B. Higher-order Magnus expansion

While the zeroth-order Magnus term $\overline{H}^{(0)}$ is often the most significant contribution to the average Hamiltonian $\overline{H}$, it is not sufficient to accurately model the time evolution. In this section, we therefore extend the analysis to the first-order Magnus approximation and full time evolution. Analytically calculating the ideal pulse parameters for the first-order Magnus approximation requires solving several challenges. Here, we lay out the general steps to computing the pulse parameters in the first-order Magnus approximation, and full details can be found in Appendix C.

First, we need to solve the double integrals in the first-order Magnus expansion in Eq. (7). We use similar methods as for the zeroth-order Magnus term to obtain infinite series expressions for these integrals, providing expressions for the drive strength Ω_I, PPP λ, and detuning Δ. These expressions form a nonlinear system of equations, which is challenging to solve. Therefore, we use fixed-point iteration to iteratively compute the pulse parameters. Even though we found this approach to numerically converge well, we found the computed pulse parameters to result in large gate errors due to non-negligible terms in the uncorrected time intervals. To resolve this problem, we split the carrier signal into a commensurate and an incommensurate term, and absorb the incommensurate term into the pulse envelopes while the commensurate term acts as the carrier signal. This enables integrating over the full gate duration at the cost of slower convergence of the infinite series expressions for the pulse parameters. We then define the ideal pulse parameters as those that minimize the error averaged over the carrier phases ϕ, which we approximate as the mean of the pulse parameters as a function of ϕ.

In Fig. 3, we numerically optimize the pulse parameters for an X_π gate for the first-order Magnus approximation and for the full time evolution and compare them with the analytically computed ideal pulse parameters. The time evolution corresponding to the first-order Magnus approximation is calculated using Eqs. (7) and (8), and the full time evolution is calculated using an ordinary differential equation solver based on the LSODA algorithm [54–56]. The cost function of the

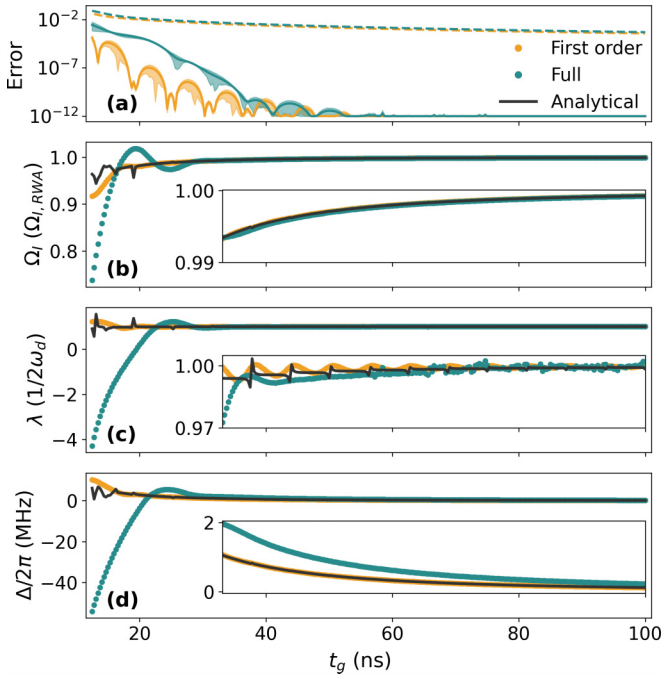

FIG. 3. (a)–(d) Optimized error, drive strength Ω_I, PPP λ, and detuning Δ, respectively, for $\omega_{01}/2\pi = 80$ MHz. The cost function for the optimizer averages over 12 different carrier phases, i.e., $N = 11$ in Eq. (15). In panel (a), the solid lines indicate the mean error and the shaded area indicates the minimum and maximum errors for the different carrier phases. The dashed lines indicate the errors for the uncorrected pulse parameters, i.e., $\mathcal{P} = \mathcal{P}_{\mathrm{RWA}}$. The analytical results plotted in panels (b)–(d) indicate the pulse parameters calculated using the approach detailed in Appendix C. The PPP in panel (c) is calculated in units of $1/2\omega_d$, where ω_d is computed using the detunings shown in panel (d). Panels (b)–(d) feature insets that enlarge the y axis for $t_g > 33$ ns. All panels, including the insets, are plotted on the same x axis shown in panel (d).

optimizer corresponds to the error averaged over a range of different carrier phases ϕ:

$$C = \sum_{k=0}^{N} (1 - F(U(\phi = \pi k/(N+1)), X_\pi)), \tag{15}$$

which ensures that the optimizer converges to pulse parameters that have a low error for all carrier phases ϕ. The optimized pulse parameters for the first-order Magnus approximation match well with the analytically computed pulse parameters for gate durations longer than 5 Magnus periods, which corresponds to approximately 30 ns for the qubit frequency used here. The drive strength and PPP of the full time evolution match well with the theoretical pulse parameters. However, the detuning is significantly higher, which we ascribe to the non-negligible influence of higher-order terms in the Magnus expansion. For gate durations shorter than 5 Magnus periods, the error increases exponentially for both the first-order Magnus approximation and the full time evolution. Additionally, the error in the full time evolution is considerably higher for these shorter gate durations, and the analytically computed pulse parameters are no longer accurate. Most likely, this occurs due to the increasing dependence of the time evolution on the carrier phase as a result from the increasing influence of higher-order terms in the Magnus expansion. We note that an analytical bound on the error between the first-order Magnus approximation and the full time evolution is challenging to compute *a priori*, as the scaling of the terms in the Magnus expansion is not well known [51,57].

We conclude that, while the first-order Magnus approximation is insufficient to accurately model the time evolution, the correction terms effectively suppress the counterrotating terms in the Hamiltonian for gate durations above 5 Magnus periods. For shorter gate durations, the dependence of the time evolution on the carrier phase becomes too significant, and as a result the gate error increases exponentially.

C. Implementing a universal gate set

Until now, we restricted our analysis to the implementation of X_π gates. For a universal gate set, it suffices to have an $X_{\pi/2}$ gate and arbitrary Z rotations [58,59]. Here, we discuss a more general case in which we allow arbitrary rotation angles about arbitrary rotation axes in the XY plane of the Bloch sphere in addition to virtual Z gates [59]. Throughout this section, we still assume the system is a perfect two-level system. The rotation axis θ is implemented by rotating the in-phase and quadrature signals according to Eq. (3). This modifies the drive term in the rotating frame according to

$$\begin{aligned} \mathcal{E}_I(t) &\mapsto \cos(\theta)\mathcal{E}_I(t) - \sin(\theta)\mathcal{E}_Q(t), \\ \mathcal{E}_Q(t) &\mapsto \cos(\theta)\mathcal{E}_Q(t) + \sin(\theta)\mathcal{E}_I(t). \end{aligned} \tag{16}$$

Following Eqs. (4) and (6) and by making the transformation $|1\rangle \mapsto e^{-i\theta}|1\rangle$, it can be shown that the requirements that need to be satisfied to minimize the error remain the same, and that only β changes according to $\beta \mapsto \beta - 2\theta$. Hence, the ideal pulse parameters are independent of the rotation axis.

From the calculations in Secs. II A and II B and Appendixes A–C, it is apparent that the ideal pulse parameters depend nonlinearly on the ratio $\Omega_I/\Omega_{I,\mathrm{RWA}}$ such that they also depend nonlinearly on the desired rotation angle. Within the RWA, the ideal drive strength is a linear function of the desired rotation angle, meaning that the determination of the drive strength for a specific rotation angle immediately gives the ideal drive strength for any other rotation angle. Beyond the RWA this no longer holds, and the ideal pulse parameters are a nontrivial function of the desired rotation angle and must be determined for each rotation angle separately.

To further emphasize the dependence of the pulse parameters on the desired rotation angle, we numerically compute the error as a function of λ and Δ in Fig. 4(a). For each point, we optimize the drive strength Ω_I according to the cost function in Eq. (15) such that each point represents the minimum achievable error for a given λ and Δ. We perform these simulations for $X_{\pi/2}$ and X_π gates and for $t_g = 40$ and 80 ns, of which the results are shown in Fig. 4(a). Even though there exists a global minimum in this parameter space, which will be close to $\lambda = 1/2\omega_{01}$ for sufficiently long gate durations, we find that there also exists a large contour on which the error is low. The existence of this contour is explained by the freedom to choose t_0 and ϕ when computing the pulse parameters. The dashed lines in Fig. 4(a) represent the ideal pulse parameters calculated using $b_- = t_0 = 0$, $b_+ = N_c t_c$ and

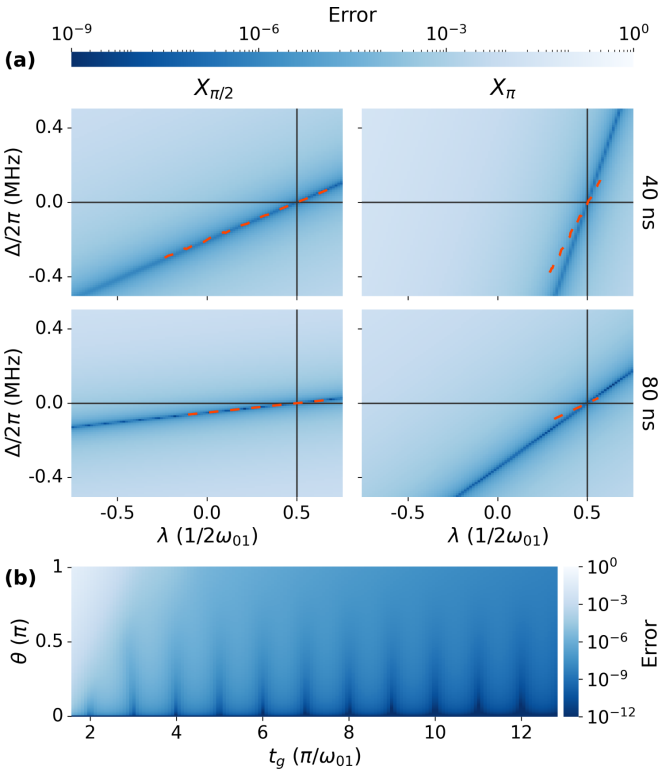

FIG. 4. (a) Minimum error vs λ and Δ for a two-level system with $\omega_{01}/2\pi = 80$ MHz. For each point, the error is minimized as a function of the drive strength Ω_t according to the cost function in Eq. (15) with $N = 12$. The first (second) row shows the results for a 40 (80) ns gate, and the first (second) column shows the results for an $X_{\pi/2}$ (X_π) gate. The crossings at $\Delta = 0$ and $\lambda = 1/4\omega_{01}$ are indicated with black solid lines. The red dashed lines indicate the analytically calculated pulse parameters corresponding to $t_0 = 0$ and varying β. (b) Error for an X_θ gate as a function of the gate duration in units of the number of Magnus periods and the rotation angle θ. For each point, we fix $\Delta = 0$ and $\lambda = 1/4\omega_d$ and the error is optimized using the same procedure as in panel (a).

along varying β. Even though this approach is not the most accurate for calculating the global minimum as done in Fig. 3, these pulse parameters still yield errors below 10^{-6} since the uncorrected time interval $t \in [N_c t_c, t_g]$ is small relative to the total gate duration. The computed pulse parameters do not align exactly with the low-error contours, which we suspect to be a result from higher-order terms in the Magnus expansion. Furthermore, they only account for a portion of the low-error contour. Other parts of the contour are explained by satisfying Eq. (6) over smaller time intervals, for instance, $b_- = t_0 = 0$ and $b_+ = (N_c - 1)t_c$.

While these contours depend on the gate duration and drive strength, Fig. 4(a) suggests that they pass through the point $\Delta = 0$, $\lambda = 1/4\omega_{01}$ independently of the gate duration and desired rotation angle. While we did not manage to prove analytically that this crossing should appear, we understand from the theory in Sec. II B and Appendix C that, if indeed the crossing exists, it should occur at $\Delta = 0$ as this indicates that the σ_z terms in the first-order Magnus expansion integrate to zero, which only leaves the zeroth-order correction terms in which λ is independent of the drive strength. To verify that this crossing exists for a wide range of parameters, we fix $\Delta = 0$ and $\lambda = 1/4\omega_{01}$ and compute the error as a function of the gate duration (in units of the number of Magnus periods) and the desired rotation angle θ in Fig. 4(b). For each point, the error is optimized using the same procedure as for Fig. 4(a). We conclude that, for gate durations as short as 5.5 Magnus periods, errors below 10^{-6} can be achieved by assuming that Δ and λ are independent of the drive strength and by finding the crossing of the low-error contours.

Finally, we highlight the usefulness of the crossing of these error contours in the context of (experimental) calibration of the pulse parameters. If the pulse parameters were calibrated by first tuning λ and Δ to an arbitrary point on the low-error contours, followed by optimization of the drive strength, the resulting error would generally not be small. This is caused by the fact that the low-error contours will move in the parameter space spanned by λ and Δ when the drive strength is changed. We recall that the dependence of the low-error contours on the drive strength is shown in Fig. 4(a). If, instead, we set $\Delta = 0$ and $\lambda = 1/4\omega_{01}$, we are at the drive strength independent point of these low-error contours, such that we can optimize the drive strength without moving off the low-error contour. This significantly reduces the complexity of (experimental) calibration of these pulse parameters, under the assumption that there is no other source of coherent errors in the system.

D. Strongly anharmonic multilevel system

In this section, we derive and verify an additional correction term to the drive pulses arising from noncomputational levels, i.e., levels $|j\rangle$ with $j \geqslant 2$. We truncate the system at four levels under the assumption that the system is strongly anharmonic and the coupling to higher levels is sufficiently weak. For a fluxonium qubit, the even transitions are parity forbidden at the operating point, such that we only have to consider drive terms for odd transitions. The drive Hamiltonian for such a system is a straightforward extension of Eq. (2) with the notable difference that we now allow the drive frequency $\omega_d(t)$ to be time-dependent. We expect that time modulating the drive frequency is in general experimentally feasible due to our assumption that the qubit frequency is low. The Hamiltonian in the rotating frame $V(t) = \exp\{i \sum_j j(\omega_d(t)t + \phi)\,|j\rangle\langle j|\}$ now becomes

$$\tilde{H}/\hbar = \sum_{0<j<4} (\omega_{0j} - j\omega_d'(t))\,|j\rangle\langle j| + \sum_{jk\in\{01,12,23,03\}} A_x^{jk}(t)\eta_{jk}\sigma_x^{jk} + A_y^{jk}(t)\eta_{jk}\sigma_y^{jk}. \quad (17)$$

Here, $\omega_d'(t) = \omega_d(t) + t\dot{\omega}_d(t)$, ω_{0j} is the energy of the jth level, and $\eta_{jk} = |\langle j|\hat{n}|k\rangle| / |\langle 0|\hat{n}|1\rangle|$ is the relative drive strength of the transition $j \leftrightarrow k$ normalized by the drive strength of the qubit transition, i.e., $\eta_{01} = 1$. In this work, we focus on charge driving such that the relative drive strengths are given by the matrix elements of the number-of-Cooper-pairs operator $\hat{n}$. Furthermore, $\sigma_x^{jk} = |j\rangle\langle k| + \text{H.c.}$, $\sigma_y^{jk} = -i\,|j\rangle\langle k| + \text{H.c.}$, $A_{x,y}^{01}(t) = A_{x,y}^{12}(t) = A_{x,y}^{23}(t) = A_{x,y}(t)$, and

$$A_x^{03}(t) = \cos(2\omega_d(t)t + 2\phi)A_x(t) - \sin(2\omega_d(t)t + 2\phi)A_y(t),$$

$$A_y^{03}(t) = \cos(2\omega_d(t)t + 2\phi)A_y(t) + \sin(2\omega_d(t)t + 2\phi)A_x(t). \tag{18}$$

The 03 drive term has a different time complexity in this frame compared to the other drive terms because it does not act on neighboring levels. We perform an adiabatic transformation to derive a first-order effective two-level Hamiltonian; see Appendix D for more details. The effect of noncomputational levels can be suppressed by setting a time-dependent detuning according to

$$\Delta'_{\mathrm{NCLs}}(t) \equiv \omega_{01} - \omega'_d(t) = \frac{\mathcal{E}_I^2(t) + \mathcal{E}_Q^2(t)}{2}\left(\frac{\eta_{12}^2}{\alpha_2} - \frac{\eta_{03}^2}{\alpha_3}\right), \tag{19}$$

with $\alpha_j = \omega_{0j} - j\omega_{01}$. The detuning has a subscript "NCLs" to highlight that it corrects for noncomputational levels and to prevent confusion with the constant detuning used in Sec. II B to correct for non-RWA errors. The corresponding detuning in the laboratory frame can be found by solving the differential equation in Eq. (19):

$$\Delta_{\mathrm{NCLs}}(t) = \frac{1}{t}\int dt\, \Delta'_{\mathrm{NCLs}}(t). \tag{20}$$

Notice that, following Eq. (16), this correction term is independent of the desired rotation angle and axis. As detailed in Appendix D, the adiabaticity parameter of this transformation is $\max\{\eta_{12}\Omega_I/\alpha_2, \eta_{03}\Omega_I/\alpha_3\}$. This implies that we strictly require the relative anharmonicity of the system to be much larger than the drive strength, i.e., $\alpha_2/\eta_{12}, \alpha_3/\eta_{03} \gg \Omega_I$. For the system studied here, $\Omega_I/2\pi \sim 100$ MHz, $\eta_{jk} \sim$ 1–20, and $\alpha_j/2\pi \sim$ 1–5 GHz. Hence, the adiabaticity parameter can approach the order of unity, which compromises the accuracy of the effective Hamiltonian. Therefore, we introduce an additional pulse parameter Ω_Δ, which rescales $\Delta_{\mathrm{NCLs}}(t)$ according to $\Delta_{\mathrm{NCLs}}(t) \mapsto \Omega_\Delta \Delta_{\mathrm{NCLs}}(t)$ or equivalently $\Delta'_{\mathrm{NCLs}}(t) \mapsto \Omega_\Delta \Delta'_{\mathrm{NCLs}}(t)$. Additionally, we allow a rescaling of the drive amplitude according to $\Omega_I \to \epsilon\Omega_I$.

To verify this correction term, we numerically minimize the error between the time-evolution operator in the computational subspace for the two-level and four-level Hamiltonians for a realistic fluxonium system as a function of Ω_Δ and ϵ. We fix $E_J/h = 5$ GHz and $E_L/h = 1$ GHz and sweep E_C to make the fluxonium heavier or lighter. We also sweep the drive strength by varying the gate duration t_g. The fluxonium energy levels and charge matrix elements corresponding to these parameters can be found in Appendix D as well as the optimized pulse parameters Ω_Δ and ϵ. In Fig. 5(a), we do not correct for the noncomputational levels by setting $\Omega_\Delta = 0$ and $\epsilon = 1$, which we refer to as the uncorrected NCL error. In Fig. 5(b), we plot the optimized error obtained by minimizing the error for each point as a function of Ω_Δ and ϵ. We find that not correcting for noncomputational levels results in errors above 10^{-4} and that the correction term in Eq. (19) can effectively suppress the influence from these levels for the majority of the parameter range. However, for short gates and heavy fluxonium parameters, the error increases sharply. We attribute this to the higher-order terms in the adiabatic transformation. In Fig. 5(c), we compute the leakage rate to noncomputational levels for the optimized pulse parameters,

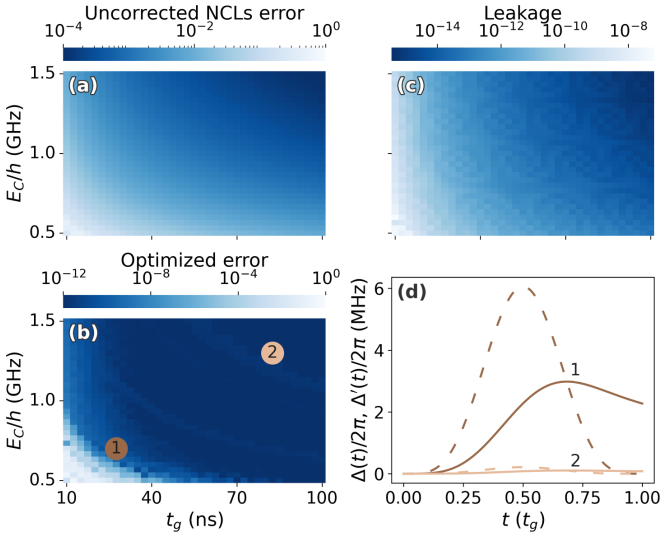

FIG. 5. Error between the time evolutions corresponding to a four-level and a two-level system for a fluxonium qubit with $E_J/h =$ 5 GHz, $E_L/h = 1$ GHz, and as a function of E_C and the gate duration t_g. The carrier phase is fixed to zero. (a) Error when not correcting for the noncomputational levels, i.e., $\Omega_\Delta = 0$ and $\epsilon = 1$. (b) Optimized error found by optimizing Ω_Δ and ϵ for each point. (c) Leakage to noncomputational states for the optimized parameters calculated using Eq. (21). (d) Optimized $\Delta(t)$ (solid lines) and $\Delta'(t)$ (dashed lines) calculated using Eqs. (19) and (20), respectively, for two points in the parameter space as indicated in panel (b). Panels (a)–(c) are plotted on the same x axis labeled in panel (b).

which we define as

$$\gamma_L(U) = \frac{1}{6}\sum_{\psi_f\in\{2,3\}}\sum_{\psi_i\in\{\pm x,\pm y,\pm z\}} |\langle\psi_f|\, U\, |\psi_i\rangle|^2. \tag{21}$$

We see that leakage is negligible for this parameter range. In Fig. 5(d), we illustrate the magnitude of the correction term by plotting the time-dependent detunings in the laboratory frame and rotating frame for four different parameters as indicated in Fig. 5(c). We emphasize that, as detailed in Appendix D, all carrier-phase-dependent terms were dropped in the derivation of the correction term in Eq. (19). In Appendix D, we investigate the dependence of the error arising from the noncomputational levels on the carrier phase, and conclude that it is negligible for the parameters used here.

We now have two corrections to the drive frequency $\omega_d(t)$: a time-independent correction Δ that corrects for the non-RWA terms as derived in Sec. II B and a time-dependent correction $\Delta_{\mathrm{NCLs}}(t)$ that corrects for the noncomputational levels as derived in this section. The combined time-dependent detuning $\Delta_{\mathrm{tot}}(t) = \Delta + \Delta_{\mathrm{NCLs}}(t)$ is a straightforward sum of these two contributions, such that we can write the time-dependent drive frequency as

$$\omega_d(t) = \omega_{01} - \Delta_{\mathrm{tot}}(t) = \omega_{01} - \Delta - \Delta_{\mathrm{NCLs}}(t). \tag{22}$$

We highlight that, in the following section, the time-independent detuning Δ is calibrated directly, while the time-dependent detuning $\Delta_{\mathrm{NCLs}}(t)$ is calibrated through the parameter Ω_Δ.

Time modulating the drive frequency comes at a cost, since the nonstationary terms in the two-level Hamiltonian also obtain a time-dependent drive frequency. In the derivation of the correction terms for the non-RWA terms in the Hamiltonian in Secs. II A and II B, we assumed that the drive frequency is time-independent. Setting a time-dependent drive frequency therefore potentially compromises the accuracy of the ideal pulse parameters calculated in this work. This challenge may be resolved by absorbing the time dependence of $\omega_d(t)$ into the pulse shapes, similar to the approach detailed in Appendix C, but we leave this for future work. We are therefore forced to assume that the drive frequency varies sufficiently slow such that we can assume that $\lambda(t) \propto 1/2\omega_d(t) = 1/2(\omega_{01} - \Delta - \Delta_{\mathrm{NCLs}}(t))$. To prevent having to time modulate λ, we absorb the time dependence into the definition of the quadrature pulse envelope by multiplying the definition of $\mathcal{E}_Q(t)$ in Eq. (9) by $(\omega_{01} - \Delta)/(\omega_{01} - \Delta - \Delta_{\mathrm{NCLs}}(t))$ and dividing λ by this same quantity:

$$\mathcal{E}_Q(t) = \lambda \frac{\partial \mathcal{E}_I(t)}{\partial t} \frac{\omega_{01} - \Delta}{\omega_{01} - \Delta - \Delta_{\mathrm{NCLs}}(t)}, \tag{23}$$

such that λ is time-independent and proportional to $1/2(\omega_{01} - \Delta)$.

III. EXPERIMENTAL IMPLEMENTATION

In a realistic experimental setting, *in situ* calibration schemes are generally required to find the optimal pulse parameters. For scalable quantum computing, it is important that these calibration schemes are efficient and experimentally inexpensive [60]. In this context, a strongly desired feature of calibration routines is that they are deterministic in the sense that they are guaranteed to minimize the gate error provided limited experimental resources. For the pulse shapes in this work, it is challenging to formulate deterministic calibration protocols, as the pulse parameters λ, Δ, and Ω_Δ all correct for coherent phase errors. Furthermore, it is not possible to optimize each parameter sequentially due to the strong interdependence of the parameters. For such pulse parameters, a popular approach is to use optimized randomized benchmarking for immediate tune-up (ORBIT) [61]. However, ORBIT is relatively resource-intensive and nondeterministic since it is based on a black-box minimization algorithm that may not converge, motivating the formulation of more efficient, deterministic calibration protocols.

To formulate deterministic calibration protocols, it is important to note that the non-RWA errors are completely determined by the shape of the pulse and not by any other system parameters. Thus, the optimal correction term can be determined prior to the experiment independently of the precise qubit parameters. The calibration could also be further simplified by discarding certain types of errors under the expectations that those errors will be small. We formulate and implement three deterministic calibration protocols (P1, P2, and P3) based on these two simplifications, and compare them against the error achieved using ORBIT, which we refer to as P4. Below, we detail each of the calibration protocols. The errors they correct for and their experimental complexity are summarized in Table I. We emphasize that none of the calibration protocols require the numerical computation of correction terms.

TABLE I. Overview of the calibration protocols. For each protocol, we indicate whether it assumes the presence of non-RWA errors or noncomputational levels, as well as an order of magnitude estimate of the number of quantum circuits (No. of q. circs.) that must be executed on the hardware as a measure of the time complexity of the protocol. We note that the precise number of circuits required depends, for instance, on the number of repetitions M of the pseudoidentity circuits and ORBIT's rate of convergence.

Protocol	Deterministic	Non-RWA errors	NCLs	No. of q. circs.
P1	✓	×	×	$\sim 10^1$
P2	✓	✓	×	$\sim 10^3$
P3	✓	Fixed	✓	$\sim 10^2$
P4	×	✓	✓	$\sim 10^4$

(1) *No errors*: We assume that there will be *no errors* from the non-RWA terms as well as from noncomputational levels such that we only need to calibrate the drive strengths Ω_I for the π and $\pi/2$ gates.

(2) *Non-RWA only*: We calibrate for the non-RWA errors by experimentally implementing the simulations shown in Fig. 4(a). We measure a heatmap of the phase error as a function of λ and Δ for the π and $\pi/2$ gates, and intersect the low-error contours to find the optimal values for λ and Δ. We still neglect the errors from noncomputational levels. We calibrate the drive strength Ω_I before and after calibrating λ and Δ.

(3) *Non-RWA and NCLs*: We make use of the fact that the non-RWA errors are completely determined by the shape of the pulse, and should not depend on any system parameters and hence do not require any calibration. We use the insights from Sec. II C and fix $\lambda = 1/4\omega_d$ and $\Delta = 0$. We then calibrate for the noncomputational levels by minimizing the phase error as a function of Ω_Δ. We calibrate the drive strength Ω_I before and after calibrating Ω_Δ.

(4) *ORBIT*: We implement ORBIT, which should find the optimal pulse parameters for the pulse shapes used in this work (as long as it is given sufficient resources and initial guesses).

In protocols P2 and P3, we measure phase errors rather than the total error [as done in Fig. 4(a)], as measuring the total gate error is experimentally expensive. To calibrate the phase errors as well as the drive strength in calibration protocols P1–P3, we make use of pseudoidentity circuits. A pseudoidentity circuit is a circuit that implements an identity when there are no errors in the operation. When there are errors, they are amplified by repeatedly applying the pseudoidentity circuit. For example, we use the pseudoidentity circuit $X_\pi - X_\pi$ to amplify over/under-rotations arising mostly from incorrectly calibrating Ω_I [62]. When repeating this circuit M times, the measured signal will oscillate as a function of M, where the oscillation amplitude and frequency depend on the magnitude of the error. Specifically, we use the difference between the maximum and minimum measured signals as a metric for the magnitude of the error. We additionally use the circuit $X_{\pi/2} - X_{\pi/2} - X_{\pi/2} - X_{\pi/2}$ to

calibrate the drive strength Ω_I for the $\pi/2$ gate. In calibration protocols P2 and P3, we use the circuits $X_\pi - Z - X_\pi - Z$ and $X_{\pi/2} - Z - X_{\pi/2} - Z$ to amplify phase errors [63]. For all circuits, the qubit is prepared in the $|0\rangle$ state. For the under/over-rotation pseudoidentity circuits, the qubit is measured in the Y basis and for the phase-error pseudoidentity circuits in the X basis.

We experimentally implement these protocols on a 98.97 MHz fluxonium qubit with average longitudinal relaxation time $T_1 = 75$ μs and Hahn echo dephasing time $T_{2E} = 37$ μs. All experiments are averaged over the carrier phase by incrementing the carrier phase by 1° in each repetition of the circuit. The protocols are implemented with gate durations t_g of 13.3, 20, 26.7, 33.3, and 40 ns. If the qubit is driven on resonance, the corresponding number of Magnus periods N_c are 2.64, 3.96, 5.28, 6.60, and 7.92. More details about the experimental setup can be found in Appendix E.

In Figs. 6(a)–6(d), we plot the phase error heatmaps for protocol P2 for $t_g = 26.7$ ns. The heatmaps for the remaining gate durations can be found in Appendix F. We also compute these heatmaps numerically and find excellent agreement with the experimental data for all gate durations. There are two key differences between the experimental heatmaps in Figs. 6(a)–6(d) and the numerical heatmaps for a two-level system in Fig. 4(a). First, multiple low-error contours appear in the experimental heatmaps, which is a result of measuring only the phase errors rather than the total gate error. Numerically, we find that only one of these contours (the ones that intersect at $\Delta = 0$) correspond to low gate errors, and the other contours arise when the phase errors are so large that they drive a full 2π rotation such that the pseudoidentity circuit implements an identity. The second key difference is that the low-error contours do not intersect at $\lambda = 1/4\omega_{01}$ but at much lower values of λ, which is a clear indication that the noncomputational levels cannot be neglected for this system. As the low-error contours still intersect at $\Delta = 0$, we optimize λ by performing a one-dimensional sweep of the phase error versus λ with $\Delta = 0$.

Figures 6(e) and 6(f) show the calibration data for protocol P3 for $t_g = 26.7$ ns. Specifically, we plot the phase error measured using the phase-error pseudoidentity circuit as a function of Ω_Δ in Fig. 6(e). We recall that Ω_Δ rescales the time-dependent detuning provided in Eq. (19), and that this correction term depends on the absolute drive strength Ω_I. Note that the experimentally optimized value of Ω_Δ may differ from the theoretically predicted value since we did not calibrate a precise conversion factor between the amplitude of the waveform generated at room temperature and the drive strength at the device. In Fig. 6(f), we plot experimental results of the phase-error pseudoidentity circuit as a function of the number of repetitions M for three points as indicated in Fig. 6(e). The green point marks the calibrated value for Ω_Δ at which the phase errors are maximally suppressed. As mentioned earlier, the phase error plotted in Fig. 6(e) is defined simply as the difference between the maximum and minimum measured points in Fig. 6(f). This definition is rather susceptible to noise in a single point, causing the phase errors in Fig. 6(e) to not drop exactly to zero.

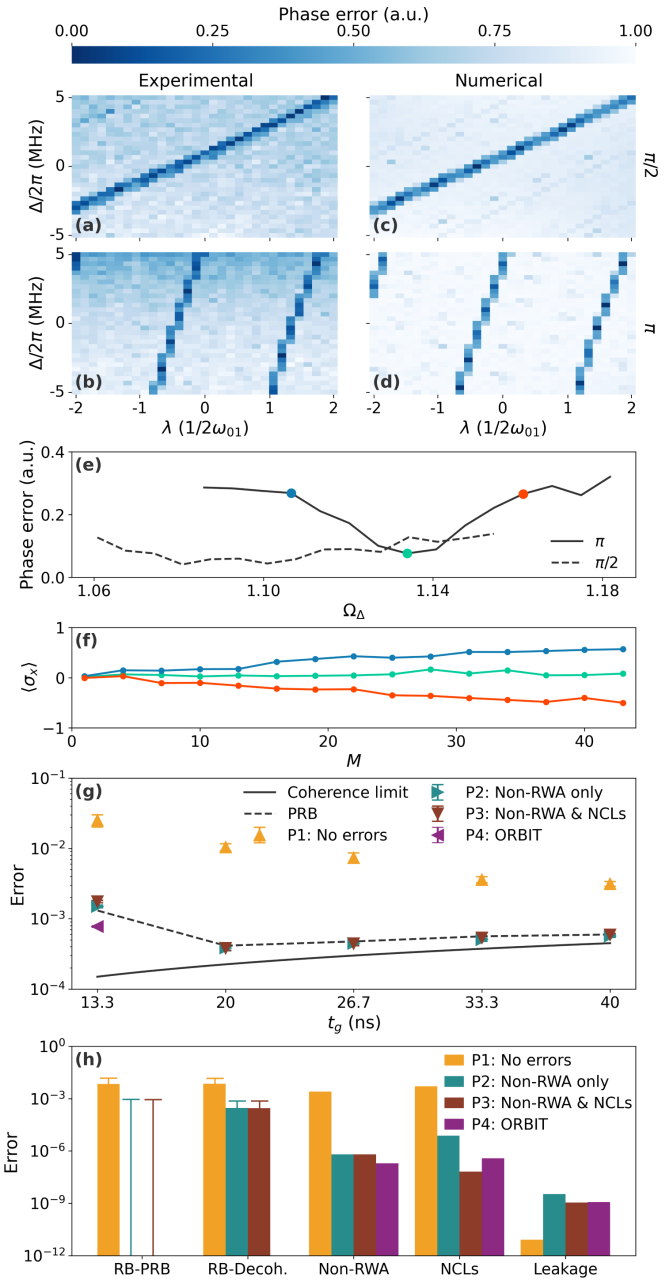

FIG. 6. (a)–(d) Heatmaps of the phase error vs λ and Δ for $t_g = 26.7$ ns. The first (second) row contains the results for the $\pi/2$ (π) gate and the first (second) column contains the experimental (numerical) results. (e) Phase error in the π and $\pi/2$ gates as a function of Ω_Δ measured for protocol P3 for $t_g = 26.7$ ns. (f) Results of the phase-error pseudoidentity circuits for three different points as indicated in panel (e). (g) Measured average gate fidelity using RB for all gate durations and protocols. The solid line indicates the coherence limit, and the dashed line indicates the measured average incoherent error for protocol P3. ORBIT has only been run for $t_g = 13.3$ ns. (h) Error budget for $t_g = 26.7$ ns. All error bars indicate one standard deviation.

To characterize the fidelity of the operations, we perform randomized benchmarking (RB) [64–66] and purity randomized benchmarking (PRB) [67] with 2^{13} repetitions

and 50 randomized Clifford sequences for each circuit depth following all calibration protocols, of which the results are shown in Fig. 6(g). RB and PRB provide the average gate fidelity and average incoherent gate fidelity, respectively, and we are most interested in the difference between these quantities as it is a measure for the magnitude of the coherent errors. We also plot the coherence limit defined by [68,69]

$$F_{\text{decoh}} = \frac{1}{2} + \frac{1}{6}\exp\left(-\frac{t_g}{T_1}\right) + \frac{1}{3}\exp\left(-\frac{t_g}{T_{2E}}\right). \tag{24}$$

From Fig. 6(g), it is apparent that the errors obtained using protocol P1 are not coherence limited, indicating that there are indeed large non-RWA errors and/or errors from noncomputational levels that should be corrected. By comparing the RB and PRB results, we see that the coherent errors for protocols P2 and P3 are negligible for $t_g \geqslant 20$ ns. However, we also notice that the errors are not coherence limited. We ascribe this to heating from the microwave pulses, as discussed in Appendix F. For $t_g = 13.3$ ns, none of the protocols achieve coherence-limited fidelities. Furthermore, we see that the incoherent error is much larger than the coherence limit for this gate duration. We attribute this to an increase in the variance of the sequence fidelities of random Clifford circuits arising from the increase in the dependence of the time evolution on the carrier phase; see also Appendix F. We only run ORBIT for $t_g = 13.3$ ns, as protocols P2 and P3 already achieve negligible coherent errors for all the other gate durations. While ORBIT improved the error compared to the deterministic calibration protocols, significant errors remain in the gate. Due to the unreliable measurement of the incoherent error for this gate duration, it is not possible to conclude whether these remaining errors are coherent or incoherent.

For each gate duration and protocol, we numerically calculate error budgets in order to estimate the minimum achievable error for each protocol and to determine whether the error is limited by non-RWA errors or noncomputational levels. To calculate these error budgets, we simulate each calibration protocol for a two-level system and for a four-level system. The resulting error for the two-level system is the error ascribed to non-RWA errors, and the difference between the errors for the four-level system and two-level system to noncomputational levels. Additionally, we calculate the leakage error for the four-level system according to Eq. (21). We do not simulate protocol P3 for a two-level system as there are no higher levels to correct for, and we simply reuse the non-RWA error from protocol P2.

The error budgets for $t_g = 26.7$ ns are plotted in Fig. 6(h) and the error budgets for the remaining gate durations can be found in Appendix F. The first data group shows the measured coherent error computed by subtracting the experimentally measured average incoherent gate fidelity from the experimentally measured average gate fidelity. Especially for the lowest gate durations, this estimate can be inaccurate due to the aforementioned increased dependence of the time evolution on the carrier phase. We therefore plot a second estimate of the coherent error in the second data group by computing the difference between the average gate fidelity and the numerically calculated decoherence error $E_{\text{decoh}} = 1 - F_{\text{decoh}}$. The accuracy of this second estimate of the coherent error is limited due to the heating effects. The remaining three data groups contain numerically computed estimates of the non-RWA errors, errors from noncomputational levels, and leakage errors, respectively. The total error rate estimated numerically is the sum of the three error rates. Even though we do not perform ORBIT experimentally for $t_g \geqslant 20$ ns, we still simulate it for all gate durations to show the minimum achievable error using the pulse shapes developed in this work.

From these error budgets, it is apparent that the error for protocol P1 consists of an almost equal combination of non-RWA errors and errors from noncomputational levels, and that the total simulated coherent error matches well with the measured coherent error. By using protocol P2, the non-RWA errors are suppressed by 1–5 orders of magnitude depending on the gate duration. The remaining error in protocol P2 is limited by errors from higher levels, even though these errors are also residually suppressed when compared to protocol P1. This indicates that the quadrature signal can, to some extent, also correct for the errors arising from the noncomputational levels. For $t_g > 20$ ns, protocol P3 can further suppress the errors from higher levels by several orders of magnitude. For shorter gate durations, we found protocol P3 to be ineffective at improving the total error. Leakage is shown to be negligible for all parameters used here. The error budgets further show that ORBIT improves the total error by approximately 1.5 and 1 orders of magnitude compared to protocols P2 and P3, respectively; see also Appendix F. This indicates that the deterministic calibration protocols are very effective at achieving errors that are close to the minimum achievable error using the pulse shapes developed in this work. Finally, the error budgets indicate that, using these deterministic calibration protocols consisting of relatively straightforward experiments, it is possible to achieve coherent error rates averaged over π and $\pi/2$ gates below 10^{-6} for $t_g \geqslant 26.7$ ns, which corresponds to 2.64 Larmor periods. We note that, as can be seen in Appendix F, these errors are strongly limited by the π gates, and we find that the error for the $\pi/2$ gates is 1–4 orders of magnitude smaller depending on the gate duration and calibration protocol. This is a result from the exponential increase in the error as the RWA becomes more invalid, as also shown in Fig. 3.

IV. OUTLOOK

In this work, we have derived and verified solutions to two challenges that arise when applying single-qubit operations in a regime where the RWA does not hold. First, the time evolution, which is now challenging to compute since the Hamiltonian is no longer self-commuting, is calculated using the Magnus expansion. We further Taylor expand the pulse envelopes and restrict the integration windows to Magnus intervals to derive expressions for the ideal pulse parameters. The second challenge is that the time evolution now depends on the carrier phase such that, in general, each operation in a sequence of gates is different. We have shown that, in the zeroth-order Magnus approximation, there exist pulse parameters that correct exactly for the counterrotating terms over the full gate duration independently of the carrier phase. This important and somewhat surprising result enables the implementation of high-fidelity operations beyond the RWA.

We further derived the ideal pulse parameters in the first-order Magnus approximation. We found that the analytically calculated ideal pulse parameters match well with the numerically optimized pulse parameters for the first-order Magnus approximation. The phase insensitivity of the correction term no longer holds in the first-order Magnus approximation. As a result, the fixed correction term used in this work can no longer correct for all coherent errors in the system, causing the error to increase for short gate durations. When using the correction terms in the full time evolution, we found that there are non-negligible effects from higher-order terms that compromise the accuracy of the calculated ideal pulse parameters. Our numerics show that the errors can be suppressed effectively in two-level systems for gate durations longer than 5 Magnus periods. For shorter operations, we found that the error increases exponentially. Achieving lower errors for gates shorter than 5 Magnus periods may be achieved by restricting to commensurate gates or by implementing circularly polarized driving [25].

While the ideal pulse parameters derived in this work are independent of the desired rotation axis, they depend strongly on the desired rotation angle. We found that a reduction in the dimensionality of the resulting optimization problem is possible due to the freedom to choose the start of the integration windows t_0 and carrier phase ϕ. This insight was fundamental for the formulation of deterministic calibration protocols in the experimental part of this work.

We derived and verified an additional correction term arising from noncomputational levels in a strongly anharmonic four-level system, inspired by the fluxonium superconducting qubit. We found that the influence from noncomputational levels can be compensated by time modulating the drive frequency. Even though the adiabaticity of the transformation that was used to derive this correction term is compromised, we found that this correction term is very effective at correcting for the influence from noncomputational levels for sufficiently high gate durations and light fluxonium parameters. Time modulating the drive frequency technically invalidates the optimal pulse parameters derived for the two-level system, since the derivations assume that the drive frequency is time-independent. This challenge may be resolved by absorbing the time dependence of the drive frequency into the definition of the pulse envelopes, but this is left for future work.

Our theoretical and numerical results enable fast tune-up of single-qubit operations on low-frequency qubits such as the fluxonium, which is crucial for scalable quantum computing. We demonstrate this experimentally on a 98.97 MHz fluxonium superconducting qubit using four calibration protocols. Notably, the experimental implementation of the pulse shapes derived in this work does not require any additional hardware or calibration complexities compared to conventional superconducting qubit measurement setups and calibration schemes. Experimentally, we achieved a minimum error rate of 3.8×10^{-4} for a gate duration corresponding to 1.98 Larmor periods. The error was limited by decoherence and heating effects from the microwave pulses. The heating effects could be mitigated by designing a less heavy fluxonium, by improving the filtering of the drive lines or by switching to flux driving. Switching to flux driving may additionally reduce the error from noncomputational levels, as the fluxonium qubit levels couple much less strongly to noncomputational levels through flux. In future work, it would be insightful to study the experimental limits of the pulse shapes and calibration protocols developed in this work on an improved device and setup.

Our numerically computed error budgets indicate that the deterministic calibration protocol P3 is the best-performing calibration protocol for the system studied in this work, as it achieves errors similar to ORBIT while requiring 2 orders of magnitude fewer quantum circuits. While it is clear from the phase-error heatmaps measured for protocol P2 that the noncomputational levels cannot be neglected for this fluxonium, it did achieve low gate errors, indicating that the non-RWA correction term can also residually suppress errors from noncomputational levels. In future work, it would be interesting to study the performance of this calibration protocol on a system that can be more accurately modeled as a two-level system, such as a fluxonium driven through its phase degree of freedom, as done in Ref. [25]. Finally, the error budgets show that, using the pulse shapes developed in this work, coherent error rates below 10^{-6} can be achieved for a gate duration of 2.64 Larmor periods, and that the remaining coherent error is a mix between non-RWA errors and errors from noncomputational levels. We were unable to verify this experimentally as these error sources both give rise to coherent phase errors. In future work, it would be insightful to derive a robust experimental methodology that can separate non-RWA errors from errors from noncomputational levels. This can further improve calibration efficiency and provide a more accurate prediction of the limiting error source in the system.

ACKNOWLEDGMENTS

The authors acknowledge the use of computational resources of the DelftBlue supercomputer, provided by Delft High Performance Computing Centre [70]. The authors further acknowledge Siyu Wang for valuable contributions to the design of the device. The authors acknowledge support from the Dutch Research Council (NWO). Additionally, E.Y.H. acknowledges support from Holland High Tech (TKI), J.H. acknowledges support from NWO Open Competition Science M, and T.V.S. acknowledges support from the Engineering and Physical Sciences Research Council (EPSRC) under EP/SO23607/1.

M.F.S.Z. performed the theoretical and numerical calculations. F.Y. designed the device. S.S., F.Y., and P.K. fabricated the device. M.F.S.Z., E.Y.H., and J.H. performed the experiments, and M.F.S.Z. analyzed the data. E.Y.H., T.V.S., and M.F.S.Z. developed and optimized the experimental setup. C.K.A. supervised the work. M.F.S.Z. wrote the manuscript with input from all authors.

DATA AVAILABILITY

All numerical and experimental data are available in Ref. [71] and the code used for the numerical simulations and data processing is available in Ref. [72].

APPENDIX A: ZEROTH-ORDER MAGNUS EXPANSION

In this Appendix, we provide a detailed derivation of the pulse shape $s_Q(t)$. The proof is inspired by the Magnus-Taylor expansion introduced in Ref. [29]. Here, we only evaluate requirement (ii) of Eq. (10) since, as we will find, the pulse shape $s_Q(t)$ does not depend on the absolute drive strength Ω_I. To satisfy requirement (ii), we need to solve integrals of the form

$$\int_{b_-}^{b_+} dt_1 T[\mathcal{E}_i(t_1), t]\cos(2\omega_d t_1 + 2\phi) = \sum_{k=0}^{\infty} \frac{\partial^k \mathcal{E}_i(t)}{\partial t^k} \int_{b_-}^{b_+} dt_1 \frac{(t_1 - t)^k}{k!} \cos(2\omega_d t_1 + 2\phi),$$
$$\int_{b_-}^{b_+} dt_1 T[\mathcal{E}_i(t_1), t]\sin(2\omega_d t_1 + 2\phi) = \sum_{k=0}^{\infty} \frac{\partial^k \mathcal{E}_i(t)}{\partial t^k} \int_{b_-}^{b_+} dt_1 \frac{(t_1 - t)^k}{k!} \sin(2\omega_d t_1 + 2\phi). \tag{A1}$$

Here, $T[\mathcal{E}_i(t_1), t]$ denotes the Taylor expansion of $\mathcal{E}_i$ at time t_1 around time t, defined as

$$T[\mathcal{E}_i(t_1), t] = \sum_{k=0}^{\infty} \frac{\partial^k \mathcal{E}_i(t)}{\partial t^k} \frac{(t_1 - t)^k}{k!}. \tag{A2}$$

The integrals in Eq. (A1) can be computed by using integration by parts, and the solutions are

$$\int_{b_-}^{b_+} dt_1 \frac{(t_1 - t)^k}{k!} \cos(2\omega_d t_1 + 2\phi) = \sum_{k'=k}^{0} \left(\frac{1}{2\omega_d}\right)^{k-k'+1} \gamma_1(k - k', \beta) \left[\frac{(t_1 - t)^{k'}}{k'!}\right]_{t_1=b_-}^{b_+} \equiv \mathcal{I}_{\mathcal{C}}(k),$$
$$\int_{b_-}^{b_+} dt_1 \frac{(t_1 - t)^k}{k!} \sin(2\omega_d t_1 + 2\phi) = -\sum_{k'=k}^{0} \left(\frac{1}{2\omega_d}\right)^{k-k'+1} \gamma_2(k - k', \beta) \left[\frac{(t_1 - t)^{k'}}{k'!}\right]_{t_1=b_-}^{b_+} \equiv \mathcal{I}_{\mathcal{S}}(k), \tag{A3}$$

with $\gamma_{1,2}(k, \beta)$ defined in Eq. (13). Substituting Eqs. (A1) and (A3) in requirement (ii) in Eq. (10) gives

$$\sum_{k=0}^{\infty} \frac{\partial^k \mathcal{E}_Q(t)}{\partial t^k} \left(\left[\frac{(t_1 - t)^{k+1}}{(k+1)!}\right]_{t_1=b_-}^{b_+} - \mathcal{I}_{\mathcal{C}}(k) \right) + \sum_{k=0}^{\infty} \frac{\partial^k \mathcal{E}_I(t)}{\partial t^k} \mathcal{I}_{\mathcal{S}}(k) = 0. \tag{A4}$$

We note that $[(t_1 - t)^{k'}/k'!]_{t_1=b_-}^{b_+} = 0$ for $k' = 0$, $\gamma_1(k+1, \beta) = \gamma_2(k, \beta)$, and

$$\mathcal{I}_{\mathcal{S}}(k+1) = -\frac{1}{2\omega_d}\mathcal{I}_{\mathcal{C}}(k) - \frac{1}{2\omega_d}\gamma_1(1, \beta)\left[\frac{(t_1 - t)^{k+1}}{(k+1)!}\right]_{t_1=b_-}^{b_+}. \tag{A5}$$

With this, we can rewrite Eq. (A4) as

$$\sum_{k=0}^{\infty} \left\{ \left[\frac{(t_1 - t)^{k+1}}{(k+1)!}\right]_{t_1=b_-}^{b_+} \left(\frac{\partial^k \mathcal{E}_Q(t)}{\partial t^k} - \frac{\gamma_1(1, \beta)}{2\omega_d} \frac{\partial^{k+1} \mathcal{E}_I(t)}{\partial t^{k+1}} \right) - \mathcal{I}_{\mathcal{C}}(k) \left(\frac{\partial^k \mathcal{E}_Q(t)}{\partial t^k} + \frac{1}{2\omega_d} \frac{\partial^{k+1} \mathcal{E}_I(t)}{\partial t^{k+1}} \right) \right\} = 0. \tag{A6}$$

From here, it is natural to set $\mathcal{E}_Q(t) = \lambda \frac{\partial \mathcal{E}_I(t)}{\partial t}$, since this allows for the straightforward derivation of a closed-form expression for λ:

$$\lambda(\mathcal{E}_I(b_+) - \mathcal{E}_I(b_-)) - \frac{\gamma_2(0, \beta)}{2\omega_d}\left[\frac{\partial^0 \mathcal{E}_I(t_1)}{\partial t_1^0}\right]_{t_1=b_-}^{b_+} - \sum_{k=0}^{\infty} \left(\frac{1}{2\omega_d}\right)^{k+1} \gamma_1(k, \beta)\left(\frac{1}{2\omega_d} + \lambda\right)\left[\frac{\partial^{k+1} \mathcal{E}_I(t)}{\partial t^{k+1}}\right]_{t_1=b_-}^{b_+}$$
$$= \lambda(\mathcal{E}_I(b_+) - \mathcal{E}_I(b_-)) - \sum_{k=0}^{\infty} \left(\frac{1}{2\omega_d}\right)^{k+1} \left\{ \lambda\gamma_1(k, \beta)\left[\frac{\partial^{k+1} \mathcal{E}_I(t)}{\partial t^{k+1}}\right]_{t_1=b_-}^{b_+} + \gamma_2(k, \beta)\left[\frac{\partial^k \mathcal{E}_I(t)}{\partial t^k}\right]_{t_1=b_-}^{b_+} \right\} = 0. \tag{A7}$$

Notice that Eq. (A7) is analogous to the result obtained in Eq. (12a).

APPENDIX B: SPECIAL PROPERTIES OF $\beta = 0$ AND SYMMETRIC INTEGRATION WINDOWS

In this Appendix, we derive the analytical solutions to Eq. (6) corresponding to $\beta = 0$ and symmetric integration windows around $t = t_g/2$. We start by deriving these solutions for $\beta = 0$ and we consider a slightly more general case in which gates start at an arbitrary time τ_0 such that the gate is applied from $t = \tau_0$ to $t = \tau_0 + t_g$. t_0 now represents the time relative to the start time of the gate such that $\beta = 2\omega_d(\tau_0 + t_0) + 2\phi$. First, we show that requirement (ii) in Eq. (10) holds for an arbitrary time interval $[t_0, t_0 + t']$. For $\beta = 0$, $\gamma_1(k, \beta)$ and $\gamma_2(k, \beta)$ are only nonzero for odd and even values of k, respectively, such that we

can rewrite Eq. (12a) as

$$\lambda(s_I(t_0+t')-s_I(t_0))=\sum_{k=0}^{\infty}\left\{(-1)^k\lambda\left(\frac{1}{2\omega_d}\right)^{2k+2}\left[\frac{\partial^{2k+2}s_I(t_1)}{\partial t_1^{2k+2}}\right]_{t_1=t_0}^{t_0+t'}+(-1)^k\left(\frac{1}{2\omega_d}\right)^{2k+1}\left[\frac{\partial^{2k}s_I(t_1)}{\partial t_1^{2k}}\right]_{t_1=t_0}^{t_0+t'}\right\}. \tag{B1}$$

We see that, if we set $\lambda=1/2\omega_d$, the first term in the sum at kth order is canceled by the second term in the sum at $(k+1)$th order. The only remaining term is the second term in the sum at $k=0$, which cancels against the term on the first line. Hence, for $\beta=0$ and $\lambda=1/2\omega_d$, requirement (ii) holds for an arbitrary interval $[t_0,t_0+t']$ in the zeroth-order Magnus approximation. For requirement (iii) in Eq. (10), we can make a similar argument. Here, we will show that, on all relevant intervals,

$$\begin{aligned}
&\text{(i)}\ \int_{\tau_0}^{\tau_0+t_0}dt_1(\mathcal{E}_I(t_1)\cos(2\omega_d t_1+2\phi)+\mathcal{E}_Q(t_1)\sin(\omega_d t_1+2\phi))=0,\\
&\text{(ii)}\ \int_{\tau_0+t_0+N_c t_c}^{\tau_0+t_g}dt_1(\mathcal{E}_I(t_1)\cos(2\omega_d t_1+2\phi)+\mathcal{E}_Q(t_1)\sin(\omega_d t_1+2\phi))=0,\\
&\text{(iii)}\ \int_{\tau_0+t_0+(n-1)t_c}^{\tau_0+t_0+nt_c}dt_1(\mathcal{E}_I(t_1)\cos(2\omega_d t_1+2\phi)+\mathcal{E}_Q(t_1)\sin(\omega_d t_1+2\phi))=0,\quad\forall\, n,
\end{aligned} \tag{B2}$$

such that, not only on the previously uncorrected intervals (i) and (ii) we require $\Omega_I=\Omega_{I,\mathrm{RWA}}$, but also on the Magnus intervals that we could correct already (iii). We first simplify the integrals with general bounds $[t_0,t_0+t']$:

$$\begin{aligned}
&\int_{t_0}^{t_0+t'}dt_1(\mathcal{E}_I(t_1)\cos(2\omega_d t_1+2\phi)+\mathcal{E}_Q(t_1)\sin(\omega_d t_1+2\phi))\\
&=\sum_{k=0}^{\infty}\left(\frac{1}{2\omega_d}\right)^{k+1}\left\{\left[\gamma_1(k,2\omega_d t_1+2\phi)\frac{\partial^k s_I(t_1)}{\partial t_1^k}\right]_{t_1=t_0}^{t_0+t'}-\lambda\left[\gamma_2(k,2\omega_d t_1+2\phi)\frac{\partial^{k+1}s_I(t_1)}{\partial t_1^{k+1}}\right]_{t_1=t_0}^{t_0+t'}\right\}\\
&=\frac{1}{2\omega_d}(\mathcal{E}_I(t_0+t')\gamma_1(0,2\omega_d(t_0+t')+2\phi)-\mathcal{E}_I(t_0)\gamma_1(0,2\omega_d t_0+2\phi))\overset{?}{=}0.
\end{aligned} \tag{B3}$$

To go from the second to the third line in Eq. (B3), we made use of the fact that $\gamma_1(k+1,\beta)=\gamma_2(k,\beta)$ such that each second term in the sum at kth order cancels with the first term in the sum at $(k+1)$th order if $\lambda=1/2\omega_d$ independently of the integration bounds. Requirement (iii) in Eq. (B2) is straightforwardly satisfied given $\beta=0$. Substituting the bounds for requirements (i) and (ii) in Eq. (B3) gives

$$\begin{aligned}
&\text{(i)}\ (\mathcal{E}_I(\tau_0+t_0)\sin(2\omega_d(\tau_0+t_0)+2\phi)-\mathcal{E}_I(\tau_0)\sin(2\omega_d\tau_0+2\phi))=0,\\
&\text{(ii)}\ (\mathcal{E}_I(\tau_0+t_g)\sin(2\omega_d(\tau_0+t_g)+2\phi)-\mathcal{E}_I(\tau_0+t_0+N_c t_c)\sin(2\omega_d(\tau_0+t_0+N_c t_c)+2\phi))=0.
\end{aligned} \tag{B4}$$

Since $\sin(2\omega_d(\tau_0+t_0))=\sin(2\omega_d(\tau_0+t_0+N_c t_c)+2\phi)=\sin(\beta)=0$, requirements (i) and (ii) in Eq. (B2) are satisfied if $\mathcal{E}_I(\tau_0)=\mathcal{E}_I(\tau_0+t_g)=0$; i.e., the pulse envelope should be zero at the start and the end of the gate. This requirement is satisfied for the cosine pulse envelopes in this work, and is generally satisfied for most pulse envelopes.

The proof for the analytical solutions to Eq. (6) in the case of symmetric integration windows follows similar steps, and relies on the assumption that $\frac{\partial^k\mathcal{E}_I(t)}{\partial t^k}$ is symmetric (antisymmetric) around $t=t_g/2$ for even (odd) k. Using this symmetry property, $\gamma_1(k+1,\beta)=\gamma_2(k,\beta)$ and $\gamma_1(k+2,\beta)=-\gamma_1(k,\beta)$, we can rewrite Eq. (12a) as

$$0=\sum_{k=0}^{\infty}\left\{\left(\frac{1}{2\omega_d}\right)^{2k+1}\lambda\gamma_1(2k,\beta)\left[\frac{\partial^{2k+1}s_I(t_1)}{\partial t_1^{2k+1}}\right]_{t_1=b_-}^{b_+}-\left(\frac{1}{2\omega_d}\right)^{2k+2}\gamma_1(2k,\beta)\left[\frac{\partial^{2k+1}s_I(t_1)}{\partial t_1^{2k+1}}\right]_{t_1=b_-}^{b_+}\right\}, \tag{B5}$$

from which it is immediately clear that all terms cancel if $\lambda=1/2\omega_d$. The symmetric (antisymmetric) terms in the remaining time intervals $t\in[\tau_0,b_-]$ and $t\in[b_+,\tau_0+t_g]$ constructively (destructively) interfere, such that we only have to consider the even time derivatives of $s_I(t)$ on one of these intervals. We now obtain

$$\lambda(s_I(b_-)-s_I(\tau_0))=\sum_{k=0}^{\infty}\left\{\left(\frac{1}{2\omega_d}\right)^{2k+2}\lambda\gamma_1(2k+1,\beta)\left[\frac{\partial^{2k+2}s_I(t_1)}{\partial t_1^{2k+2}}\right]_{t_1=\tau_0}^{b_-}+\left(\frac{1}{2\omega_d}\right)^{2k+1}\gamma_1(2k+1,\beta)\left[\frac{\partial^{2k}s_I(t_1)}{\partial t_1^{2k}}\right]_{t_1=\tau_0}^{b_-}\right\}. \tag{B6}$$

Similarly as for Eq. (B1), if we set $\lambda=1/2\omega_d$, all terms in the sum cancel against each other except for the second term at $k=0$, which cancels against the term on the first line. To show that we additionally require $\Omega_I=\Omega_{I,\mathrm{RWA}}$ on all three intervals, we can readily use Eq. (B3). We immediately see that Eq. (B3) is satisfied by substituting the bounds of the three intervals, adding the terms together, employing the symmetry of $s_I(t)$ around $t=t_g/2$, and by using that $s_I(\tau_0)=s_I(\tau_0+t_g)=0$.

Finally, we comment on an important difference between the analytical solutions for $\beta = 0$ and symmetric integration windows. For the analytical solutions corresponding to $\beta = 0$, the RWA and non-RWA time evolutions intersect at $t = t_0 + nt_c$ for each n and also at the end of the gate, as also apparent from Fig. 2(d). For the analytical solutions corresponding to symmetric integration windows this is not the case, and the only guarantee is that the time evolutions intersect at the end of the gate. This difference in behavior arises from the fact that for $\beta = 0$ the non-RWA terms in the time evolution are actually corrected *in real time* by the pulse parameters. However, for the symmetric integration windows this is not the case, as the asymmetric terms in the time interval $t \in [\tau_0, b_-]$ cancel against those in the time interval $t \in [b_+, \tau_0 + t_g]$.

APPENDIX C: FIRST-ORDER MAGNUS EXPANSION

In this Appendix, we calculate the pulse parameters in the first-order Magnus approximation. This involves solving slightly more complicated expressions compared to the zeroth-order Magnus approximation. For example, for the detuning Δ we need to solve

$$\frac{\Delta}{2} m t_c \sigma_z = -\frac{i}{2}\int_{b_-}^{b_+} dt_1 \int_{b_-}^{t_1} dt_1 [A_I(t_1)\sigma_x + A_Q(t_1)\sigma_y, A_I(t_2)\sigma_x + A_Q(t_2)\sigma_y] = \int_{b_-}^{b_+} dt_1 \int_{b_-}^{t_1} dt_1 (A_I(t_1)A_Q(t_2) - A_Q(t_1)A_I(t_2))\sigma_z. \tag{C1}$$

Here, we again use general bounds $b_- = t_0 + (n-m)t_c$ and $b_+ = t_0 + nt_c$. The double integrals in Eq. (C1) are computed using the same approach as in the zeroth-order Magnus approximation in order to obtain expressions for the integrals as infinite series. Importantly, the terms in these sums now scale with $(2/N_c)^k$ compared to $(1/N_c)^k$ in the zeroth-order Magnus terms. This change in scaling arises from terms such as $\mathcal{E}_I^2(t) \sim \cos(4\pi t/t_g)$, which oscillate twice as fast as the original pulse envelope terms. Consequently, the pulse parameters can only be calculated for $N_c > 2$, as for $N_c \leqslant 2$ the terms in these sums do not converge. This logic extends to higher-order Magnus terms, since the nth-order Magnus term contains terms such as $\mathcal{E}_I^n(t) \propto \cos(2(n+1)\pi t/t_g)$. Hence, to derive the pulse parameters in the nth-order Magnus approximation, we require $N_c > n+1$ to ensure all the infinite series converge. This does not imply that solutions for the ideal pulse parameters do not exist in the nth-order Magnus approximation for $N_c \leqslant n+1$. For example, it is possible to evaluate the integrals in Eq. (C1) for $N_c < 2$ using a similar approach but by swapping the roles of the oscillating terms and pulse envelopes in integration by parts such that the terms in the infinite series scale with $(N_C/2)^k$.

To compute the first-order correction terms, we make use of the following general solutions to the double integrals in Eq. (C1):

$$\begin{aligned}
&\int_{b_-}^{b_+} dt_1 f(t_1) \int_{b_-}^{t_1} dt_2 g(t_2) \sin(2\omega_d t_2 + 2\phi) \\
&= \sum_{k_1=0}^{\infty} \left(\frac{1}{2\omega_d}\right)^{k_1+1} \gamma_2(k_1,\beta) \frac{\partial^{k_1} g(t)}{\partial t^{k_1}}\bigg|_{t=b_-} \int_{b_-}^{b_+} dt_1 f(t_1) \\
&\quad - \sum_{k_1=0}^{\infty}\sum_{k_2=0}^{\infty} \left(\frac{1}{2\omega_d}\right)^{2+k_1+k_2} (-1)^{\lfloor \frac{k_1+2}{2} \rfloor} (\chi_+(k_1)\gamma_1(k_2,\beta) - \chi_-(k_1)\gamma_2(k_2,\beta)) \left[\frac{\partial^{k_2}}{\partial t^{k_2}}\left(f(t)\frac{\partial^{k_1} g(t)}{\partial t^{k_1}}\right)\right]_{t=b_-}^{b_+},
\end{aligned} \tag{C2a}$$

$$\begin{aligned}
&\int_{b_-}^{b_+} dt_1 f(t_1) \int_{b_-}^{t_1} dt_2 g(t_2) \cos(2\omega_d t_2 + 2\phi) \\
&= -\sum_{k_1=0}^{\infty} \left(\frac{1}{2\omega_d}\right)^{k_1+1} \gamma_1(k_1,\beta) \frac{\partial^{k_1} g(t)}{\partial t^{k_1}}\bigg|_{t=b_-} \int_{b_-}^{b_+} dt_1 f(t_1) \\
&\quad + \sum_{k_1=0}^{\infty}\sum_{k_2=0}^{\infty} \left(\frac{1}{2\omega_d}\right)^{2+k_1+k_2} (-1)^{\lfloor \frac{k_1}{2} \rfloor} (\chi_-(k_1)\gamma_1(k_2,\beta) - \chi_+(k_1)\gamma_2(k_2,\beta)) \left[\frac{\partial^{k_2}}{\partial t^{k_2}}\left(f(t)\frac{\partial^{k_1} g(t)}{\partial t^{k_1}}\right)\right]_{t=b_-}^{b_+},
\end{aligned} \tag{C2b}$$

$$\begin{aligned}
&\int_{b_-}^{b_+} dt_1 g(t_1) \sin(2\omega_d t_1 + 2\phi) \int_{b_-}^{t_1} dt_2 f(t_2) \\
&= -\sum_{k=0}^{\infty} \left(\frac{1}{2\omega_d}\right)^{k+1} \gamma_2(k,\beta) \left(\left[\frac{\partial^k}{\partial t^k}(g(t)f^{(1)}(t))\right]_{t=b_-}^{b_+} - f^{(1)}(b_-)\left[\frac{\partial^k g(t)}{dt^k}\right]_{t=b_-}^{b_+}\right),
\end{aligned} \tag{C2c}$$

$$\begin{aligned}
&\int_{b_-}^{b_+} dt_1 g(t_1) \cos(2\omega_d t_1 + 2\phi) \int_{b_-}^{t_1} dt_2 f(t_2) \\
&= \sum_{k=0}^{\infty} \left(\frac{1}{2\omega_d}\right)^{k+1} \gamma_1(k,\beta) \left(\left[\frac{\partial^k}{\partial t^k}(g(t)f^{(1)}(t))\right]_{t=b_-}^{b_+} - f^{(1)}(b_-)\left[\frac{\partial^k g(t)}{dt^k}\right]_{t=b_-}^{b_+}\right),
\end{aligned} \tag{C2d}$$

$$\int_{b_-}^{b_+} dt_1 \int_{b_-}^{t_1} dt_2 f(t_1)\sin(2\omega_d t_1 + 2\phi) g(t_2)\sin(2\omega_d t_2 + 2\phi)$$
$$= \sum_{k=0}^{\infty} -\frac{(-1)^{\lfloor \frac{k-1}{2} \rfloor}}{2}\left(\frac{1}{2\omega_d}\right)^{k+1} \chi_-(k) \int_{b_-}^{b_+} dt f(t) \frac{\partial^k g(t)}{\partial t^k}$$
$$+ \sum_{k_1=0}^{\infty}\sum_{k_2=0}^{\infty}\left(\frac{1}{2\omega_d}\right)^{k_1+k_2+2}\left\{\left(\frac{1}{2}\right)^{k_1+2}(\chi_-(k_2)\gamma_1(k_1,2\beta) + \chi_+(k_2)\gamma_2(k_1,2\beta))\left[\frac{\partial^{k_1}}{\partial t^{k_1}}\left(f(t)\frac{\partial^{k_2} g(t)}{\partial t^{k_2}}\right)\right]_{t=b_-}^{b_+}\right.$$
$$\left. - \gamma_2(k_1,\beta)\gamma_2(k_2,\beta)\frac{\partial^{k_2} g(t)}{\partial t^{k_2}}\bigg|_{t=b_-}\left[\frac{\partial^{k_1} f(t)}{\partial t^{k_1}}\right]_{t=b_-}^{b_+}\right\}, \tag{C2e}$$

$$\int_{b_-}^{b_+} dt_1 \int_{b_-}^{t_1} dt_2 f(t_1)\sin(2\omega_d t_1 + 2\phi) g(t_2)\cos(2\omega_d t_2 + 2\phi)$$
$$= \sum_{k=0}^{\infty} \frac{(-1)^{\lfloor \frac{k}{2} \rfloor}}{2}\left(\frac{1}{2\omega_d}\right)^{k+1} \chi_+(k) \int_{b_-}^{b_+} dt f(t) \frac{\partial^k g(t)}{\partial t^k}$$
$$+ \sum_{k_1=0}^{\infty}\sum_{k_2=0}^{\infty}\left(\frac{1}{2\omega_d}\right)^{k_1+k_2+2}\left\{\left(\frac{1}{2}\right)^{k_1+2}(-\chi_+(k_2)\gamma_1(k_1,2\beta) - \chi_-(k_2)\gamma_2(k_1,2\beta))\left[\frac{\partial^{k_1}}{\partial t^{k_1}}\left(f(t)\frac{\partial^{k_2} g(t)}{\partial t^{k_2}}\right)\right]_{t=b_-}^{b_+}\right.$$
$$\left. + \gamma_2(k_1,\beta)\gamma_1(k_2,\beta)\frac{\partial^{k_2} g(t)}{\partial t^{k_2}}\bigg|_{t=b_-}\left[\frac{\partial^{k_1} f(t)}{\partial t^{k_1}}\right]_{t=b_-}^{b_+}\right\}, \tag{C2f}$$

$$\int_{b_-}^{b_+} dt_1 \int_{b_-}^{t_1} dt_2 f(t_1)\cos(2\omega_d t_1 + 2\phi) g(t_2)\sin(2\omega_d t_2 + 2\phi)$$
$$= \sum_{k=0}^{\infty} -\frac{(-1)^{\lfloor \frac{k-1}{2} \rfloor}}{2}\left(\frac{1}{2\omega_d}\right)^{k+1} \chi_+(k) \int_{b_-}^{b_+} dt f(t) \frac{\partial^k g(t)}{\partial t^k}$$
$$+ \sum_{k_1=0}^{\infty}\sum_{k_2=0}^{\infty}\left(\frac{1}{2\omega_d}\right)^{k_1+k_2+2}\left\{\left(\frac{1}{2}\right)^{k_1+2}(-\chi_+(k_2)\gamma_1(k_1,2\beta) + \chi_-(k_2)\gamma_2(k_1,2\beta))\left[\frac{\partial^{k_1}}{\partial t^{k_1}}\left(f(t)\frac{\partial^{k_2} g(t)}{\partial t^{k_2}}\right)\right]_{t=b_-}^{b_+}\right.$$
$$\left. + \gamma_1(k_1,\beta)\gamma_2(k_2,\beta)\frac{\partial^{k_2} g(t)}{\partial t^{k_2}}\bigg|_{t=b_-}\left[\frac{\partial^{k_1} f(t)}{\partial t^{k_1}}\right]_{t=b_-}^{b_+}\right\}, \tag{C2g}$$

$$\int_{b_-}^{b_+} dt_1 \int_{b_-}^{t_1} dt_2 f(t_1)\cos(2\omega_d t_1 + 2\phi) g(t_2)\cos(2\omega_d t_2 + 2\phi)$$
$$= \sum_{k=0}^{\infty} \frac{(-1)^{\lfloor \frac{k}{2} \rfloor}}{2}\left(\frac{1}{2\omega_d}\right)^{k+1} \chi_-(k) \int_{b_-}^{b_+} dt f(t) \frac{\partial^k g(t)}{\partial t^k}$$
$$+ \sum_{k_1=0}^{\infty}\sum_{k_2=0}^{\infty}\left(\frac{1}{2\omega_d}\right)^{k_1+k_2+2}\left\{\left(\frac{1}{2}\right)^{k_1+2}(\chi_-(k_2)\gamma_1(k_1,2\beta) - \chi_+(k_2)\gamma_2(k_1,2\beta))\left[\frac{\partial^{k_1}}{\partial t^{k_1}}\left(f(t)\frac{\partial^{k_2} g(t)}{\partial t^{k_2}}\right)\right]_{t=b_-}^{b_+}\right.$$
$$\left. - \gamma_1(k_1,\beta)\gamma_1(k_2,\beta)\frac{\partial^{k_2} g(t)}{\partial t^{k_2}}\bigg|_{t=b_-}\left[\frac{\partial^{k_1} f(t)}{\partial t^{k_1}}\right]_{t=b_-}^{b_+}\right\}. \tag{C2h}$$

Here, $g^{(1)}(t)$ denotes the first antiderivative of $g(t)$. Solving for the ideal pulse parameters using these general solutions is still challenging, since Eq. (C2) together with Eq. (12) forms a very nonlinear system of equations. For example, the integrals in Eq. (C2) define the detuning, but they themselves depend on the detuning since the integration windows depend on ω_d as well as Ω_I and λ that depend on ω_d in a similar way. Therefore, we use fixed-point iteration to obtain the pulse parameters, which we find to converge well.

After solving and numerically verifying the correction terms in the first-order Magnus approximation, we found the calculated pulse parameters to be highly inaccurate. This is caused by non-negligible effects from terms outside the integration windows, i.e., with $t \in [0, t_0] \cup [t_0 + N_c t_c, t_g]$. We find this effect to be most prominent in the first-order corrections

to λ. Consider, for example, the term

$$\zeta_1(b_-, b_+) = \frac{\Delta}{2}\int_{b_-}^{b_+} dt_1 \int_{b_-}^{t_1} dt_2(\mathcal{E}_I(t_1) - \mathcal{E}_I(t_2)). \quad \text{(C3)}$$

This term integrates exactly to zero over the entire duration of the gate, i.e., $\zeta_1(0, t_g) = 0$, but is nonzero and on the same order as the correction terms in the zeroth-order Magnus approximation for other values of b_- and b_+. This severely compromises the accuracy of the calculated ideal pulse parameters, as we are effectively correcting for a term that trivially integrates to zero. To resolve this issue, we split the carrier signal into two terms: one term that is commensurate with the gate duration and a term that is incommensurate. We then absorb the incommensurate term into the pulse envelopes and define the commensurate term as the carrier signal. This enables integrating over the full time evolution for arbitrary gate durations and drive frequencies at the cost of slower convergence of the infinite series expressions for the pulse parameters. Concretely, we rewrite

$$\begin{aligned}
&\mathcal{E}(t)\cos(2\omega_d t + 2\phi)\\
&\quad = \mathcal{E}(t)(\cos(2\hat{\omega}_d t + 2\hat{\phi})\cos(2\tilde{\omega}_d t + 2\tilde{\phi})\\
&\qquad - \sin(2\hat{\omega}_d t + 2\hat{\phi})\sin(2\tilde{\omega}_d t + 2\tilde{\phi})),\\
&\mathcal{E}(t)\sin(2\omega_d t + 2\phi)\\
&\quad = \mathcal{E}(t)(\sin(2\hat{\omega}_d t + 2\hat{\phi})\cos(2\tilde{\omega}_d t + 2\tilde{\phi})\\
&\qquad + \cos(2\hat{\omega}_d t + 2\hat{\phi})\sin(2\tilde{\omega}_d t + 2\tilde{\phi})). \quad \text{(C4)}
\end{aligned}$$

Here, the oscillating terms $\propto\hat{\omega}_d$ take the role of carrier signal, while we absorb the oscillating terms $\propto\tilde{\omega}_d$ into the pulse envelope, here denoted in a general form as $\mathcal{E}(t)$. We also redefine the carrier phase to ensure that the updated pulse envelopes maintain the (anti)symmetric properties of their derivatives around $t = t_g/2$, although this is not strictly necessary. More specifically, we have $\hat{N}_c = \lfloor t_g\omega_d/\pi \rceil$, $\hat{\omega}_d = \pi\hat{N}_c/t_g$, $\tilde{\omega}_d = \omega_d - \hat{\omega}_d$, $\tilde{\phi} = -\tilde{\omega}_d t_g/2$, and $\hat{\phi} = \phi + \tilde{\omega}_d t_g/2$. Here, $\lfloor\cdot\rceil$ denotes rounding to the nearest integer. Notice that $|\tilde{\omega}_d| \leqslant \pi/2t_g$, such that the infinite series expressions will still converge as long as $N_c > 2$ for the zeroth-order Magnus approximation and $N_c > 3$ for the first-order Magnus approximation. The pulse parameters calculated in Fig. 3 are computed up to 15th order in $3/N_c$. Using this substitution, we can force the carrier signal to be commensurate with the gate duration, such that we can always integrate over the full gate duration and we are no longer limited by Magnus intervals. While it may seem as if we effectively lose the t_0 degree of freedom here, this is not the case. This degree of freedom is expressed through the choice of dividing the total carrier phase ϕ between $\tilde{\phi}$ and $\hat{\phi}$. Here, this division is fixed to maintain the symmetry properties of the pulse envelopes. To compute the ideal pulse parameters, we need to minimize the gate error averaged over all carrier phases as a function of the pulse parameters; i.e., we need to solve $\min_{\mathcal{P}(\phi)} \mathbb{E}_\phi[\text{Error}(\phi)]$. This is highly nontrivial, and we simply compute the ideal pulse parameters by averaging over the carrier phases: $\mathcal{P} = \mathbb{E}_\phi[\mathcal{P}(\phi)]$.

APPENDIX D: MODELING A STRONGLY ANHARMONIC SYSTEM AS A TWO-LEVEL SYSTEM

Modeling a strongly anharmonic system, such as the fluxonium, as a two-level system requires the derivation of an effective Hamiltonian in the computational subspace of the four-level Hamiltonian given in Eq. (17). We perform an adiabatic elimination using

$$\begin{aligned}
\tilde{H}_{\text{eff}}(t) &= e^{-iS(t)}\tilde{H}(t)e^{iS(t)} + \frac{\partial S(t)}{\partial t}\\
&= \tilde{H}(t) - i[S(t), \tilde{H}(t)] + \frac{1}{2}[S(t), [S(t), \tilde{H}(t)]] + \ldots\\
&\quad + \frac{\partial S(t)}{\partial t},\\
S(t) &= -\frac{\eta_{12}A_y(t)}{\alpha_2}\sigma_x^{12} + \frac{\eta_{12}A_x(t)}{\alpha_3}\sigma_y^{12}\\
&\quad - \frac{\eta_{03}A_y^{03}(t)}{\alpha_3}\sigma_x^{03} + \frac{\eta_{03}A_x^{03}(t)}{\alpha_3}\sigma_y^{03}. \quad \text{(D1)}
\end{aligned}$$

Neglecting terms $\mathcal{O}(S^2)$ and higher, the effective Hamiltonian becomes

$$\begin{aligned}
\tilde{H}_{\text{eff}}(t) &= (\omega_1 - \omega_d' + \Delta'(t))\,|1\rangle\langle 1|\\
&\quad + \sum_{jk\in\{01,02,13\}} A_x^{jk}(t)\eta_{ij}\sigma_x^{jk} + A_y^{jk}(t)\eta_{jk}\sigma_y^{jk},\\
\Delta'(t) &= \frac{\mathcal{E}_I^2(t) + \mathcal{E}_Q^2(t)}{2}\left(\frac{\eta_{03}^2}{\alpha_3} - \frac{\eta_{12}^2}{\alpha_2}\right), \quad \text{(D2)}
\end{aligned}$$

where we have neglected all nonstationary terms in $\Delta'(t)$. Notice that $\Delta'(t)$ in Eq. (D2) is equal to Eq. (19) up to a change in sign. Here, we have essentially solved the opposite problem compared to the main text: We calculated how the drive terms in the two-level Hamiltonian change due to the effect from higher levels. However, we are interested in the opposite problem: How do we need to change the pulse parameters in the four-level Hamiltonian such that we can model the system by the two-level Hamiltonian in Eq. (4), explaining the change in sign.

Notice that, due to the strong coupling of the higher-order transitions in the fluxonium qubit, the adiabaticity of this transformation is compromised, as $|\mathcal{E}_I(t)\eta_j/\alpha_j|$ can approach the order of unity. This explains why the error in Fig. 5(b) is large for short gate durations and heavy fluxonium parameters.

In the main text, we optimized Ω_Δ and ϵ such that we can model the fluxonium by a two-level system as a function of the gate duration and E_C. In Figs. 7(a) and 7(b), we plot the fluxonium parameters belonging to this range of E_C's. In Figs. 7(c) and 7(d), we plot the fitted parameters Ω_Δ and ϵ. We see that, for the majority of the parameter range, the fitted parameters are close to 1, showing that the adiabatic transformation derived in this section effectively captures the effect from higher-order levels for this parameter range.

In deriving Eq. (D2), we dropped all nonstationary drive terms. In addition to being nonstationary, these terms also depend on the carrier phase ϕ. Importantly, these terms are not dropped in our numerical evaluation of the time evolution, and the optimized error plotted in Fig. 5(b) and the corresponding

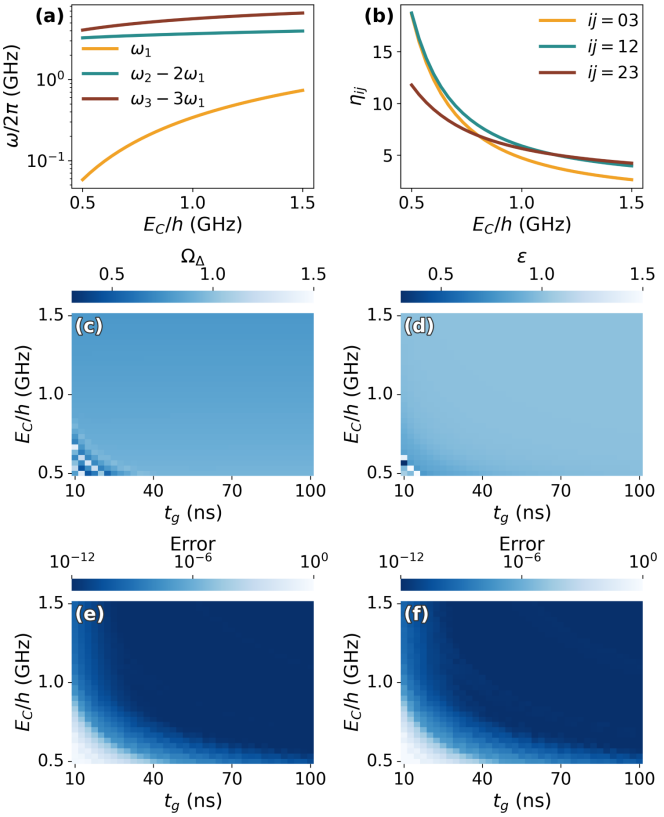

FIG. 7. Fluxonium parameters and pulse parameters for the results shown in Fig. 5. Panels (a) and (b) show the energy levels and relative drive strengths as a function of E_C, respectively. Panels (c) and (d) show the optimized parameters Ω_Δ and ϵ, respectively. In panels (e) and (f), we show the dependence of the error on the carrier phase. For each point, we use the pulse parameters optimized for the carrier phase $\phi = 0$ shown in panels (c) and (d), and compute the error for a range of 12 carrier phases. The mean and maximum error for this range of carrier phases are plotted in panels (e) and (f), respectively.

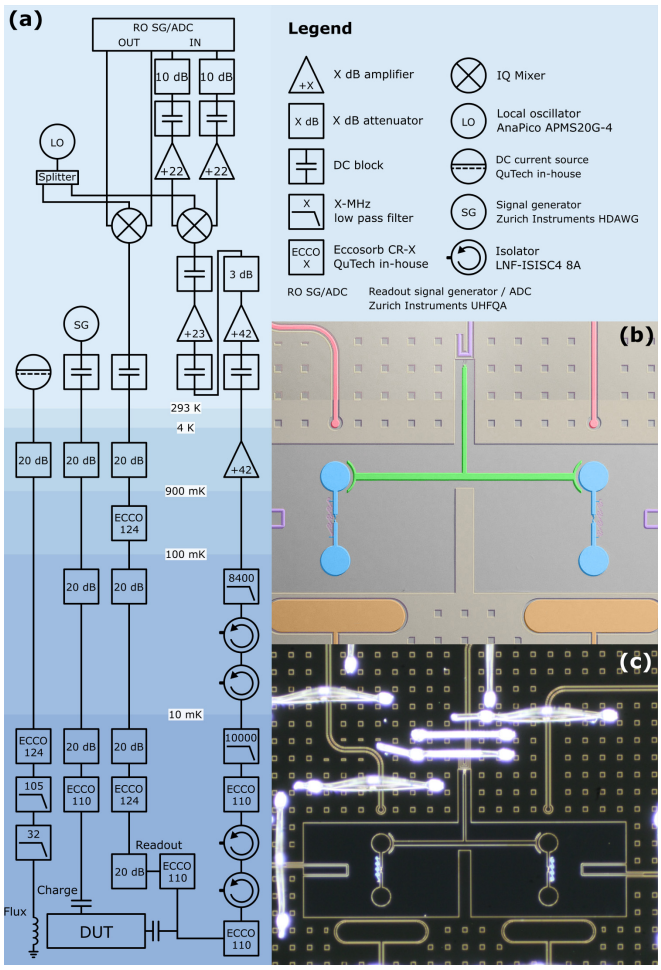

FIG. 8. (a) Schematic of the electronic setup used in the experiments. (b) False-colored image of the device. The two fluxonium qubits are shown in blue, and the tunable transmon in green. The charge and flux lines are shown in pink and purple, respectively, and the pad of the readout resonator is shown in brown. (c) Optical microscope image of the fabricated device.

optimized pulse parameters shown in Figs. 7(c) and 7(d) were specifically calculated for $\phi = 0$. To investigate the additional error arising from these terms, we plot the mean and maximum error as a function of the carrier phase in Figs. 7(e) and 7(f). For each point, we use the optimized pulse parameters for $\phi = 0$ shown in Figs. 7(c) and 7(d), and calculate the error for a range of $N = 12$ carrier phases selected according to Eq. (15). We see that for low values of E_C, corresponding to heavy fluxoniums with a qubit frequency below 100 MHz, an additional small error arises from the carrier-phase-dependent drive terms. When comparing Figs. 7(e) and 7(f) to Fig. 5(b), we see that the carrier-phase dependence only marginally influences the threshold in terms of t_g and E_C at which the error from noncomputational levels is above 10^{-6}.

APPENDIX E: DEVICE AND EXPERIMENTAL SETUP

The fluxonium qubit on which the experiments were performed was part of a two-fluxonium system in which the fluxoniums are coupled by a tunable transmon. We experimentally obtained the fluxonium's energy parameters as $E_C/h = 0.88$ GHz, $E_L/h = 0.50$ GHz, and $E_J/h = 4.92$ GHz. The fluxonium is capacitively coupled to a 4.993 GHz resonator used for dispersive readout. For more details on the device, we refer the reader to Ref. [73]. A false-colored image of the device is shown in Fig. 8(b) and an optical microscope image is shown in Fig. 8(c). During these experiments, both fluxoniums were parked at $\varphi_{\text{ext}} = 0.5$ and the transmon was at a flux bias point that suppressed the residual zz interaction between the fluxoniums. Specifically, we measure a residual zz interaction of 0.5 ± 2 kHz.

The device was cooled down in a Bluefors LD400 dilution refrigerator to a base temperature of 8 mK. The device is protected from electromagnetic noise by an aluminum shield that is placed directly on top of the printed circuit board. The device is further protected from thermal and electromagnetic noise by one copper can and two MuMETAL cans. The full electronic setup is

displayed in Fig. 8(a). To flux-bias the qubits, we use an in-house made DC current generator. The qubit drive pulses were generated by a Zurich Instruments HDAWG at a sampling rate of 2.4 GS/s. Given the low frequency of the fluxonium qubit, no upconversion of the drive pulses is required. Due to the challenges with microwave heating in this experiment, we do not use an active reset such as a sideband reset [43]. Instead, we make use of postselection, in which each circuit is preceded by a measurement to determine the state of the qubit at the start of the circuit. To counteract heating from the drive pulses, this initial measurement is preceded by a delay time of 700 µs. There is another 7 µs delay between the initial measurement and the start of the actual circuit to ensure the readout resonator is depleted again. The readout pulses are generated and analyzed by the Zurich Instruments UHFQA. They are upconverted using the Zurich Instruments HDIQ mixer with an LO signal from the AnaPico APMS20G-4. All signals pass through a series of filters, attenuators, and in-house made Eccosorb IR filters. The output signal passes through a series of cryogenic dual-junction isolators, a cryogenic HEMT (LNF-LNC4_8C), a room-temperature HEMT (LNF-LNR4_8ART), and through a 23-dB amplifier (Mini-Circuits ZRON-8G+) before being demodulated and passing through one more amplifier (Mini-Circuits GALI-3+).

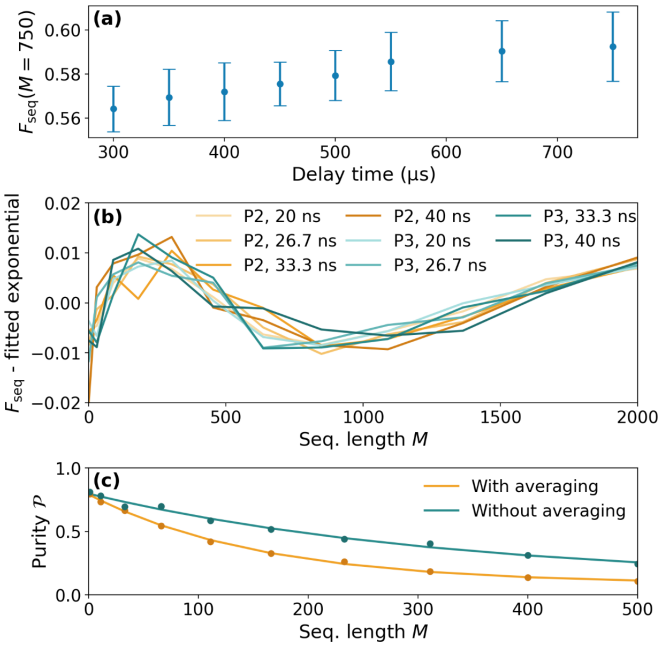

FIG. 9. (a) RB sequence fidelity for $M = 750$ and $t_g = 20$ ns as a function of the initial delay time. (b) Difference between the measured sequence fidelities and the fitted exponential decay curve for all RB measurements of protocols P2 and P3 with $t_g \geqslant 20$ ns. (c) Purity RB decay curves for $t_g = 13.3$ ns with and without averaging each circuit over the carrier phase. The markers indicate the measured data, and the solid line the fitted exponential decay curve.

APPENDIX F: EXTENDED DATA

1. Heating and incoherent errors

Here, we elaborate on the discrepancy between the incoherent error rate measured using PRB and the expected incoherent error from decoherence processes. For $t_g \geqslant 20$ ns, we suspect that the majority of the discrepancy arises from heating from the microwave pulses. To verify this, we measure the RB sequence fidelity for a sequence length of $M = 750$ and for $t_g = 20$ ns as a function of the delay time before the postselection measurement, of which the results are shown in Fig. 9(a). We see that the sequence fidelity improves by increasing the delay time, which is very typical for microwave heating. For the experiments presented in this work, the delay time was fixed to 700 µs. However, we found that significant effects from heating remained. To highlight this, we plot the difference between the measured RB sequence fidelities and the fitted exponential decay curve for the RB experiments performed for protocols P2 and P3 and for all gate durations $t_g \geqslant 20$ ns in Fig. 9(b). We see that the data consistently deviate from an exponential decay curve. The sequence fidelities for short sequence lengths are higher than the fitted exponential decay, whereas the sequence fidelity for longer sequences is lower than the fitted exponential decay. This is an indication that there is still significant heating from the microwave pulses that increases the error rate as a function of the sequence length.

For the 13.3 ns gate, the discrepancy between the incoherent error measured using PRB and estimated from decoherence is much higher than that for the other gate durations. We ascribe this to the increased dependence of the time evolution on the carrier phase. PRB essentially measures the decay of the variance of the sequence fidelities of random Clifford circuits. It takes advantage of the fact that incoherent errors reduce this variance, while coherent errors do not. For an increasing amount of non-RWA errors, the dependence of the time evolution on the carrier phase also increases. We suspect that, since we average each circuit over the carrier phase by incrementing the carrier phase by 1° for each repetition of the circuit, this increasing dependence on the carrier phase amounts to an increase in the decay of the variance of the sequence fidelities. To verify this, we measure PRB for a 13.3 ns gate in Fig. 9(c) with and without averaging over the carrier phases. Specifically, we plot the normalized purity $\mathcal{P} = \sqrt{\langle\sigma_x\rangle^2 + \langle\sigma_y\rangle^2 + \langle\sigma_z\rangle^2}$ versus the sequence length M. If we average over the carrier phase, we measure an incoherent error rate of 1.7×10^{-3}. By disabling this averaging and measuring each circuit only for one specific carrier phase, the measured incoherent error rate improves significantly to 0.8×10^{-3}. We conclude that the increase in the variance of the coherent error compromises the accuracy of the incoherent error rate measured using PRB.

2. Phase-error heatmaps

In Fig. 10, we plot the phase-error heatmaps for the remaining gate durations. We plot heatmaps for π rotations as well as for $\pi/2$ rotations. We further verified these

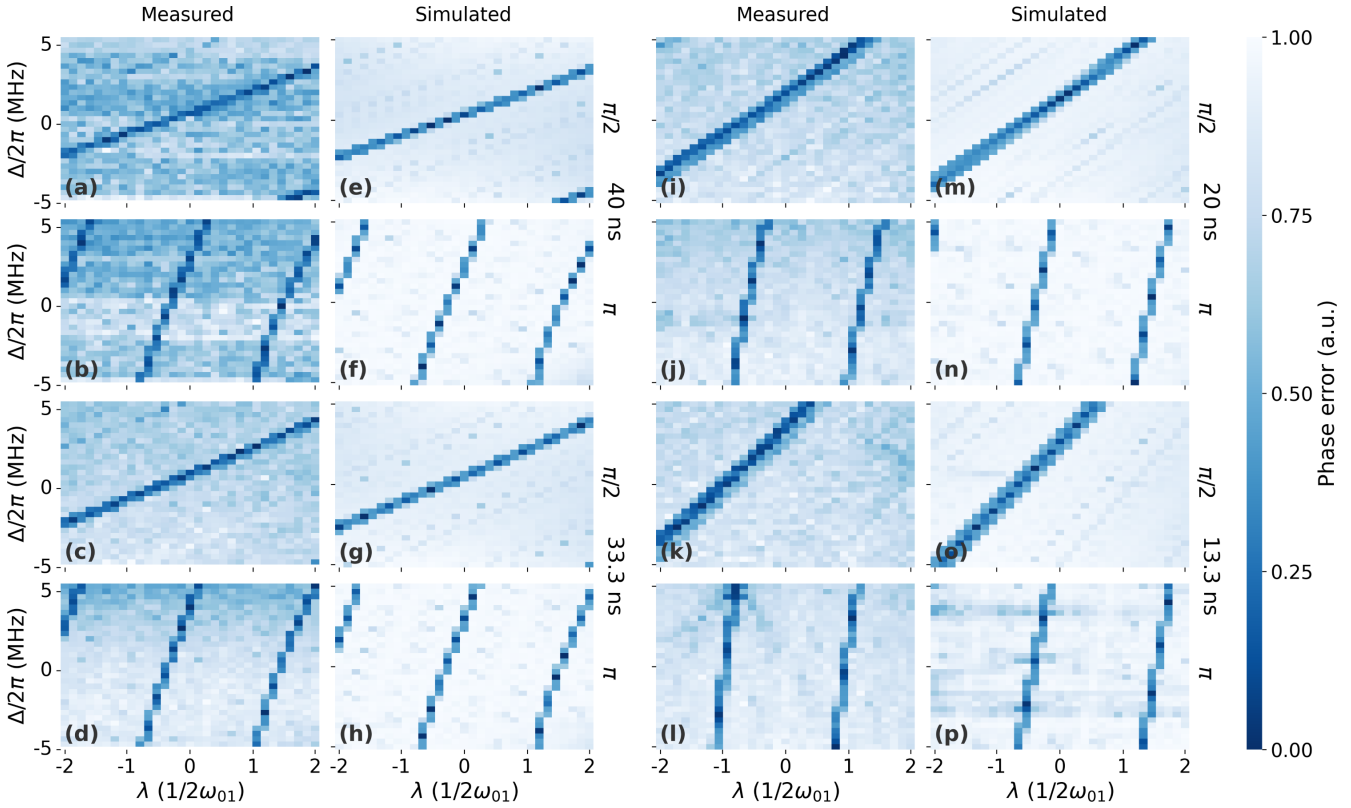

FIG. 10. (a)–(d), (i)–(l) All remaining experimental heatmaps and (e)–(h), (m)–(p) all the remaining numerical heatmaps of the phase error as a function of the PPP λ and the detuning Δ, respectively. Panels (a), (b), (e), and (f) contain the results for the 40 ns gate; panels (c), (d), (g), and (h) for the 33.3 ns gate; panels (i), (j), (m), and (n) for the 20 ns gate; and panels (k), (l), (o), and (p) for the 13.3 ns gate. Panels (a), (c), (e), (g), (i), (k), (m), and (o) contain results for the $\pi/2$ gates, and panels (b), (d), (f), (h), (j), (l), (n), and (p) for the π gates.

heatmaps by simulating the experiments numerically. We find very good correspondence between the experimental and numerical heatmaps. Simulating the phase-error pseudoidentity circuits raises a computational challenge. If the RWA holds, each operation only needs to be solved once for a specified value of λ and Δ. Here, due to the dependence of the time evolution on the carrier phase, every operation in a circuit is different and needs to be simulated separately. Since we additionally average the experimentally executed circuits over the initial carrier phase, simulating these experiments is a computationally expensive task. Therefore, for each gate duration, we numerically solve the four-level time evolution for a set range of 41 values for the detuning Δ, PPP λ, and carrier phase ϕ each. We then truncate the time evolution to the qubit subspace and fit the rotation angle and axis. We linearly interpolate those values to obtain the time evolution for arbitrary values of Δ, λ, and ϕ. This significantly reduces the total number of time evolutions that need to be solved to approximately 1.4 million, for which we make use of an high-performance cluster [70].

3. Error budgets

Figures 11(a)–11(e) show the error budgets for all protocols and all gate durations. The procedure for computing the error budgets is outlined in the main text. Figure 11(f) shows the total estimated coherent error for π and $\pi/2$ gates individually. Depending on the gate duration and calibration protocol, the $\pi/2$ gates achieve coherent errors that are 1–4 orders of magnitude smaller than the π gates. This is ascribed to the exponential increase in the coherent error when the RWA becomes increasingly invalid. Therefore, it is possible to achieve lower coherent errors for shorter gate durations by using a universal gate set that is made up of only $\pi/2$ gates. Finally, Fig. 11 shows that the deterministic calibration protocols P2 and P3 achieve error rates averaged over the π and $\pi/2$ gates that are typically within 1.5 and 1 orders of magnitude of the errors computed with protocol P4, respectively. This shows that the deterministic calibration protocols are very effective at achieving error rates that are close to the minimum achievable error using the pulse shapes developed in this work.

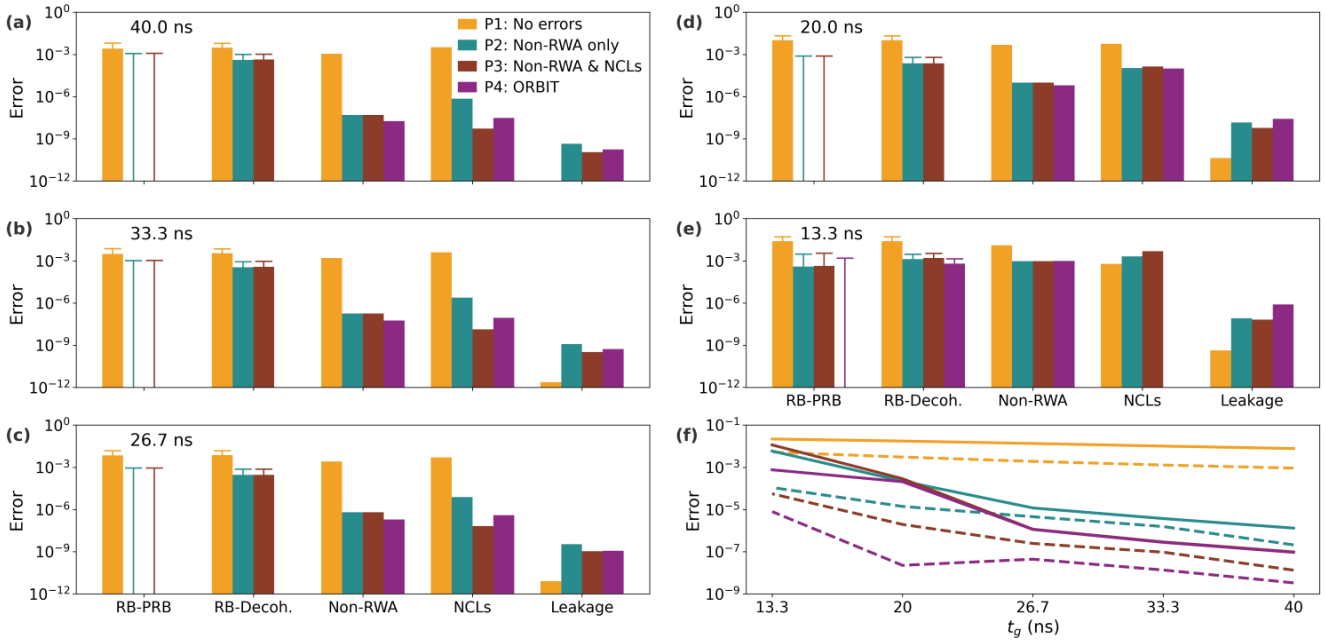

FIG. 11. (a)–(e) Error budgets for all gate durations. (f) Total estimated coherent error for the $\pi/2$ gates (dashed lines) and π gates (solid lines). Panels (a)–(e) are plotted on the same x axes labeled in panels (c) and (e).

[1] M. A. Nielsen and I. L. Chuang, *Quantum Computation and Quantum Information* (Cambridge University Press, Cambridge, 2010).

[2] J. Preskill, Quantum computing in the NISQ era and beyond, Quantum **2**, 79 (2018).

[3] H. P. Bartling, J. Yun, K. N. Schymik, M. Van Riggelen, L. A. Enthoven, H. B. Van Ommen, M. Babaie, F. Sebastiano, M. Markham, D. J. Twitchen, and T. H. Taminiau, Universal high-fidelity quantum gates for spin-qubits in diamond, Phys. Rev. Appl. **23**, 034052 (2025).

[4] S. G. J. Philips, M. T. Mądzik, S. V. Amitonov, S. L. De Snoo, M. Russ, N. Kalhor, C. Volk, W. I. L. Lawrie, D. Brousse, L. Tryputen, B. P. Wuetz, A. Sammak, M. Veldhorst, G. Scappucci, and L. M. K. Vandersypen, Universal control of a six-qubit quantum processor in silicon, Nature (London) **609**, 919 (2022).

[5] F. Borsoi, N. W. Hendrickx, V. John, M. Meyer, S. Motz, F. Van Riggelen, A. Sammak, S. L. De Snoo, G. Scappucci, and M. Veldhorst, Shared control of a 16 semiconductor quantum dot crossbar array, Nat. Nanotechnol. **19**, 21 (2024).

[6] T. P. Harty, D. T. C. Allcock, C. J. Ballance, L. Guidoni, H. A. Janacek, N. M. Linke, D. N. Stacey, and D. M. Lucas, High-fidelity preparation, gates, memory, and readout of a trapped-ion quantum bit, Phys. Rev. Lett. **113**, 220501 (2014).

[7] M. C. Smith, A. D. Leu, K. Miyanishi, M. F. Gely, and D. M. Lucas, Single-qubit gates with errors at the 10^{-7} level, Phys. Rev. Lett. **134**, 230601 (2025).

[8] M. Kjaergaard, M. E. Schwartz, J. Braumüller, P. Krantz, J. I.-J. Wang, S. Gustavsson, and W. D. Oliver, Superconducting qubits: Current state of play, Annu. Rev. Condens. Matter Phys. **11**, 369 (2020).

[9] P. Krantz, M. Kjaergaard, F. Yan, T. P. Orlando, S. Gustavsson, and W. D. Oliver, A quantum engineer's guide to superconducting qubits, Appl. Phys. Rev. **6**, 021318 (2019).

[10] I. I. Rabi, Space quantization in a gyrating magnetic field, Phys. Rev. **51**, 652 (1937).

[11] I. I. Rabi, J. R. Zacharias, S. Millman, and P. Kusch, A new method of measuring nuclear magnetic moment, Phys. Rev. **53**, 318 (1938).

[12] S. H. Autler and C. H. Townes, Stark effect in rapidly varying fields, Phys. Rev. **100**, 703 (1955).

[13] F. Motzoi and F. K. Wilhelm, Improving frequency selection of driven pulses using derivative-based transition suppression, Phys. Rev. A **88**, 062318 (2013).

[14] C. J. Wood and J. M. Gambetta, Quantification and characterization of leakage errors, Phys. Rev. A **97**, 032306 (2018).

[15] F. Motzoi, J. M. Gambetta, P. Rebentrost, and F. K. Wilhelm, Simple pulses for elimination of leakage in weakly nonlinear qubits, Phys. Rev. Lett. **103**, 110501 (2009).

[16] J. M. Gambetta, F. Motzoi, S. T. Merkel, and F. K. Wilhelm, Analytic control methods for high-fidelity unitary operations in a weakly nonlinear oscillator, Phys. Rev. A **83**, 012308 (2011).

[17] Z. Chen, J. Kelly, C. Quintana, R. Barends, B. Campbell, Y. Chen, B. Chiaro, A. Dunsworth, A. G. Fowler, E. Lucero *et al.*, Measuring and suppressing quantum state leakage in a superconducting qubit, Phys. Rev. Lett. **116**, 020501 (2016).

[18] B. Li, T. Calarco, and F. Motzoi, Experimental error suppression in cross-resonance gates via multi-derivative pulse shaping, npj Quantum Inf. **10**, 66 (2024).

[19] E. Hyyppä, A. Vepsäläinen, M. Papič, C. F. Chan, S. Inel, A. Landra, W. Liu, J. Luus, F. Marxer, C. Ockeloen-Korppi, S. Orbell, B. Tarasinski, and J. Heinsoo, Reducing leakage of

single-qubit gates for superconducting quantum processors using analytical control pulse envelopes, PRX Quantum **5**, 030353 (2024).

[20] N. Khaneja, T. Reiss, C. Kehlet, T. Schulte-Herbrüggen, and S. J. Glaser, Optimal control of coupled spin dynamics: Design of nmr pulse sequences by gradient ascent algorithms, J. Magn. Reson. **172**, 296 (2005).

[21] M. Werninghaus, D. J. Egger, F. Roy, S. Machnes, F. K. Wilhelm, and S. Filipp, Leakage reduction in fast superconducting qubit gates via optimal control, npj Quantum Inf. **7**, 14 (2021).

[22] F. Bloch and A. Siegert, Magnetic resonance for nonrotating fields, Phys. Rev. **57**, 522 (1940).

[23] A. Laucht, S. Simmons, R. Kalra, G. Tosi, J. P. Dehollain, S. Freer, F. E. Hudson, K. M. Itoh, D. N. Jamieson, J. C. McCallum, A. S. Dzurak, and A. Morello, Breaking the rotating wave approximation for a strongly driven dressed single-electron spin, Phys. Rev. B **94**, 161302(R) (2016).

[24] L. Biró and A. Csehi, Time-dependent state populations with and without the rotating wave approximation: A model-based study, J. Mod. Opt. **66**, 119 (2019).

[25] D. A. Rower, L. Ding, H. Zhang, M. Hays, J. An, P. M. Harrington, I. T. Rosen, J. M. Gertler, T. M. Hazard, B. M. Niedzielski *et al.*, Suppressing counter-rotating errors for fast single-qubit gates with fluxonium, PRX Quantum **5**, 040342 (2024).

[26] S. Ahn, K. Park, D. Cho, M. Lim, T. Choi, and A. S. Moskalenko, Single-qubit quantum gate at an arbitrary speed, arXiv:2412.19561.

[27] J. Scheuer, X. Kong, R. S. Said, J. Chen, A. Kurz, L. Marseglia, J. Du, P. R. Hemmer, S. Montangero, T. Calarco, B. Naydenov, and F. Jelezko, Precise qubit control beyond the rotating wave approximation, New J. Phys. **16**, 093022 (2014).

[28] J. J. Cáceres, D. Domíngues, and M. J. Sánches, Fast quantum gates based on Landau-Zener-Stückelberg-Majorana transitions, Phys. Rev. A **108**, 052619 (2023).

[29] D. Zeuch, F. Hassler, J. J. Slim, and D. P. DiVincenzo, Exact rotating wave approximation, Ann. Phys. **423**, 168327 (2020).

[30] V. E. Manucharyan, J. Koch, L. I. Glazman, and M. H. Devoret, Fluxonium: Single Cooper-pair circuit free of charge offsets, Science **326**, 113 (2009).

[31] P. Groszkowski and J. Koch, Scqubits: A python package for superconducting qubits, Quantum **5**, 583 (2021).

[32] S. P. Chitta, T. Zhao, Z. Huang, I. Mondragon-Shem, and J. Koch, Computer-aided quantization and numerical analysis of superconducting circuits, New J. Phys. **24**, 103020 (2022).

[33] K. N. Nesterov, I. V. Pechenezhskiy, C. Wang, V. E. Manucharyan, and M. G. Vavilov, Microwave-activated controlled-z gate for fixed-frequency fluxonium qubits, Phys. Rev. A **98**, 030301(R) (2018).

[34] L. B. Nguyen, Y.-H. Lin, A. Somoroff, R. Mencia, N. Grabon, and V. E. Manucharyan, High-coherence fluxonium qubit, Phys. Rev. X **9**, 041041 (2019).

[35] K. N. Nesterov, C. Wang, V. E. Manucharyan, and M. G. Vavilov, Cnot gates for fluxonium qubits via selective darkening of transitions, Phys. Rev. Appl. **18**, 034063 (2022).

[36] I. N. Moskalenko, I. A. Simakov, N. N. Abramov, A. A. Grigorev, D. O. Moskalev, A. A. Pishchimova, N. S. Smirnov, E. V. Zikiy, I. A. Rodionov, and I. S. Besedin, High fidelity two-qubit gates on fluxoniums using a tunable coupler, npj Quantum Inf. **8**, 130 (2022).

[37] F. Bao, H. Deng, D. Ding, R. Gao, X. Gao, C. Huang, X. Jiang, H. S. Ku, Z. Li, X. Ma *et al.*, Fluxonium: An alternative qubit platform for high-fidelity operations, Phys. Rev. Lett. **129**, 010502 (2022).

[38] L. B. Nguyen, G. Koolstra, Y. Kim, A. Morvan, T. Chistolini, S. Singh, K. N. Nesterov, C. Jünger, L. Chen, Z. Pedramrazi, B. K. Mitchell, J. M. Kreikebaum, S. Puri, D. I. Santiago, and I. Siddiqi, Blueprint for a high-performance fluxonium quantum processor, PRX Quantum **3**, 037001 (2022).

[39] A. Somoroff, Q. Ficheux, R. A. Mencia, H. Xiong, R. Kuzmin, and V. E. Manucharyan, Millisecond coherence in a superconducting qubit, Phys. Rev. Lett. **130**, 267001 (2023).

[40] I. A. Simakov, G. S. Mazhorin, I. N. Moskalenko, N. N. Abramov, A. A. Grigorev, D. O. Moskalev, A. A. Pishchimova, N. S. Smirnov, E. V. Zikiy, I. A. Rodionov, and I. S. Besedin, Coupler microwave-activated controlled-phase gate on fluxonium qubits, PRX Quantum **4**, 040321 (2023).

[41] E. Dogan, D. Rosenstock, L. Le Guevel, H. Xiong, R. A. Mencia, A. Somoroff, K. N. Nesterov, M. G. Vavilov, V. E. Manucharyan, and C. Wang, Two-fluxonium cross-resonance gate, Phys. Rev. Appl. **20**, 024011 (2023).

[42] L. Ding, M. Hays, Y. Sung, B. Kannan, J. An, A. Di Paolo, A. H. Karamlou, T. M. Hazard, K. Azar, D. K. Kim *et al.*, High-fidelity, frequency-flexible two-qubit fluxonium gates with a transmon coupler, Phys. Rev. X **13**, 031035 (2023).

[43] T. Wang, F. Wu, F. Wang, X. Ma, G. Zhang, J. Chen, H. Deng, R. Gao, R. Hu, L. Ma *et al.*, Efficient initialization of fluxonium qubits based on auxiliary energy levels, Phys. Rev. Lett. **132**, 230601 (2024).

[44] T. V. Stefanski, F. Yilmaz, E. Y. Huang, M. F. S. Zwanenburg, S. Singh, S. Wang, L. J. Splitthoff, and C. K. Andersen, Improved fluxonium readout through dynamic flux pulsing, arXiv:2411.13437.

[45] F. Yilmaz, S. Singh, M. F. S. Zwanenburg, J. Hu, T. V. Stefanski, and C. K. Andersen, Energy participation ratio analysis for very anharmonic superconducting circuits, arXiv:2411.15039.

[46] Q. Ficheux, L. B. Nguyen, A. Somoroff, H. Xiong, K. N. Nesterov, M. G. Vavilov, and V. E. Manucharyan, Fast logic with slow qubits: Microwave-activated controlled-z gate on low-frequency fluxoniums, Phys. Rev. X **11**, 021026 (2021).

[47] B.-L. Najera-Santos, R. Rousseau, K. Gerashchenko, H. Patange, A. Riva, M. Villiers, T. Briant, P.-F. Cohadon, A. Heidmann, J. Palomo *et al.*, High-sensitivity ac-charge detection with a mhz-frequency fluxonium qubit, Phys. Rev. X **14**, 011007 (2024).

[48] H. Zhang, C. Ding, D. K. Weiss, Z. Huang, Y. Ma, C. Guinn, S. Sussman, S. P. Chitta, D. Chen, A. A. Houck, J. Koch, and D. I. Schuster, Tunable inductive coupler for high-fidelity gates between fluxonium qubits, PRX Quantum **5**, 020326 (2024).

[49] A. Blais, A. L. Grimsmo, S. M. Girvin, and A. Wallraff, Circuit quantum electrodynamics, Rev. Mod. Phys. **93**, 025005 (2021).

[50] W. Magnus, On the exponential solution of differential equations for a linear operator, Commun. Pure Appl. Math. **7**, 649 (1954).

[51] S. Blanes, F. Casa, J. A. Oteo, and J. Ros, The Magnus expansion and some of its applications, Phys. Rep. **470**, 151 (2009).

[52] M. D. Bowdrey, D. K. L. Oi, A. J. Short, K. Banaszek, and J. A. Jones, Fidelity of single qubit maps, Phys. Lett. A **294**, 258 (2002).

[53] L. H. Pedersen, N. M. Møller, and K. Mølmer, Fidelity of quantum operations, Phys. Lett. A **367**, 47 (2007).

[54] L. Petzold, Automatic selection of methods for solving stiff and nonstiff systems of ordinary differential equations, SIAM J. Sci. Stat. Comput. **4**, 136 (1983).

[55] A. C. Hindmarsh, ODEPACK, a systematized collection of ODE solver, in *Scientific Computing, IMACS Transactions on Scientific Computation*, edited by R. S. Stepleman, M. Carver, R. Peskin, W. F. Ames, and R. Vichnevetsky (North-Holland, Amsterdam, 1983), Vol. 1, p. 55–64.

[56] P. Virtanen, R. Gommers, T. E. Oliphant, M. Haberland, T. Reddy, D. Cournapeau, E. Burovski, P. Peterson, W. Weckesser, J. Bright *et al.*, Scipy 1.0: Fundamental algorithms for scientific computing in Python, Nat. Methods **17**, 261 (2020).

[57] F. Casas, Sufficient conditions for the convergence of the Magnus expansion, J. Phys. A: Math. Theor. **40**, 15001 (2007).

[58] C. P. Williams, *Explorations in Quantum Computing* (Springer, London, 2011), Chap. 2, pp. 51–122.

[59] D. C. McKay, C. J. Wood, S. Sheldon, J. M. Chow, and J. M. Gambetta, Efficient z gates for quantum computing, Phys. Rev. A **96**, 022330 (2017).

[60] M. Mohseni, A. Schere, K. G. Johnson, O. Wertheim, M. Otten, N. A. Aadit, Y. Alexeev, K. M. Bresniker, K. Y. Camsari, B. Chapman *et al.*, How to build a quantum supercomputer: Scaling from hundreds to millions of qubits, arXiv:2411.10406.

[61] J. Kelly, B. Barends, B. Campbell, Y. Chen, Y. Chen, B. Chiaro, A. Dunsworth, A. G. Fowler, I.-C. Hoi, E. Jeffrey *et al.*, Optimal quantum control using randomized benchmarking, Phys. Rev. Lett. **112**, 240504 (2014).

[62] S. Lazar, Improving single-qubit gates in superconducting quantum devices, Ph.D. thesis, ETH Zurich, 2023.

[63] E. Lucero, J. Kelly, R. C. Bialczak, M. Lenander, M. Mariantoni, M. Neeley, A. D. O'Connell, D. Sank, H. Wang, M. Weides, J. Wenner, T. Yamamoto, A. N. Cleland, and J. M. Martinis, Reduced phase error through optimized control of a superconducting qubit, Phys. Rev. A **82**, 042339 (2010).

[64] E. Knill, D. Leibfried, R. Reichle, J. Britton, R. B. Blakestad, J. D. Jost, C. Langer, R. Ozeri, S. Seidelin, and D. J. Wineland, Randomized benchmarking of quantum gates, Phys. Rev. A **77**, 012307 (2008).

[65] E. Magesan, J. M. Gambetta, and J. Emerson, Scalable and robust randomized benchmarking of quantum processes, Phys. Rev. Lett. **106**, 180504 (2011).

[66] E. Magesan, J. M. Gambetta, and J. Emerson, Characterizing quantum gates via randomized benchmarking, Phys. Rev. A **85**, 042311 (2012).

[67] J. Wallman, C. Granade, R. Harper, and S. T. Flammia, Estimating the coherence of noise, New J. Phys. **17**, 113020 (2015).

[68] S. Asaad, C. Dickel, N. K. Langford, S. Poletto, A. Bruno, M. A. Rol, D. Deurloo, and L. DiCarlo, Independent, extensible control of same-frequency superconducting qubits by selective broadcasting, npj Quantum Inf. **2**, 16029 (2016).

[69] J. Heinsoo, Digital quantum computation with superconducting qubits, Ph.D. thesis, ETH Zurich, 2019.

[70] Delft High Performance Computing Center (DHPC), DelftBlue supercomputer (phase 2) (2024).

[71] Data repository, https://doi.org/10.4121/4e5a545d-436b-4d59-86d2-61506ccaf3cf.

[72] GitHub repository, https://github.com/andersenqubitlab/single-qubit-gates-beyond-the-rwa.

[73] S. Singh, E. Y. Huang, J. Hu, F. Yilmaz, M. F. S. Zwanenburg, P. Kumaravadivel, S. Wang, T. V. Stefanski, and C. K. Andersen, Fast microwave-driven two-qubit gates between fluxonium qubits with a transmon coupler, arXiv:2504.13718.